Thermoplastic modification of polycrystalline copper surface microstructure by nonmelting nanosecond laser pulses

I. V. Nelasov,[1, 2, *] S. S. Manokhin,[1] Yu. R. Kolobov,[1] V. V. Zhakhovsky,[3, †] S. Yu. Grigoryev,[3] E. A. Perov,[4] Yu. V. Petrov,[5] V. A. Khokhlov,[5] N. A. Inogamov,[5, 3, 6] Y. V. Khomich,[7] T. V. Malinskiy,[7] and V. E. Rogalin[7, ‡]

[1] *Federal Research Center of Problems of Chemical Physics and Medicinal Chemistry, RAS, 1 Semenova av., 142432 Chernogolovka, Russia*
[2] *Lomonosov Moscow State University, Moscow 119991, Russia*
[3] *Dukhov Research Institute of Automatics, 22 Sushchevskaya st., 127030 Moscow, Russia*
[4] *Institute for Computer Aided Design of Russian Academy of Sciences, 2nd Brestskaya St., 19/18, 123056, Moscow, Russia*
[5] *Landau Institute for Theoretical Physics, RAS, 1A Semenova av., 142432 Chernogolovka, Russia*
[6] *Joint Institute for High Temperatures, RAS, 13/2 Izhorskaya st., 125412 Moscow, Russia*
[7] *Institute for Electrophysics and Electric Power of Russian Academy of Sciences (IEE RAS) Dvorcovaya naberezhnaya, 18, Litera A, 191181, Saint Petersburg, Russia*

Mechanisms of surface relief formation on bulk polycrystalline oxygen-free copper samples under single and multiple UV nanosecond laser pulses (355 nm, 10 ns) in air are investigated. The laser spot size $\sim 100\,\mu$m is several times larger than the average size $\sim 40\,\mu$m of crystal grains. Incident fluences are limited by $\sim 1\,\mathrm{J/cm^2}$ to avoid melting of copper. Confocal laser microscopy, scanning electron microscopy, and transmission electron microscopy are utilized to reveal the deformation processes leading to surface relief development. It is found that irradiation uncovers the grain boundaries on the exposed surface. Dislocation subboundaries and packets of nanoscale plates of deformation twins near the grain boundaries are observed in a subsurface layer of 20–100 nm thick.

According to our theoretical analysis and simulations, the observed surface modification is caused by nonuniform plastic deformation of crystallites induced by nonmelting laser heating. Continuum modeling of such heating shows that the shockwave effects are negligible since the generated acoustic waves have pressure less than 100 atm. We demonstrate that the solid copper goes to the plastic deformation regime if the temperature rise exceeds ~ 250 degrees. Atomistic simulation of polycrystals reveals anisotropy of grain deformation and asynchronous plastic response due to their different stiffness depending on lattice orientation, as well as the residual stresses and growth of surface roughness after each heating–cooling cycle.

The obtained results are important for understanding the physical mechanisms of surface degradation of copper mirrors under laser induced thermocycling.

I. INTRODUCTION

The study of pulsed laser processing of metallic materials is currently a rapidly developing field of fundamental research, the results of which are finding increasing practical applications [1–6]. Further progress in this field is largely determined by advances in understanding the physical mechanisms of phase-structural transformations in subsurface layers and surface relief formation, which significantly affect the optical, chemical and mechanical properties of metal parts [7–12].

The growing interest in this area is primarily due to the development of new practical methods for surface hardening and increasing plasticity [3–6, 13], the possibility of achieving extreme wettability characteristics [14, 15], precision external surface treatment (including improving the optical damage resistance of high-power mirror, such as laser mirrors [12, 16]), and optimizing the thermal regimes of high-frequency microelectronic components. Such components are subjected to thermocycling due to intense heat exchange. In engineering, the mismatch of thermal expansion coefficients of contacting materials (e.g. silicon chips, substrates, and solders) causes deformations, cracks, and fractures in joints. As a result, fatigue processes under cyclic stresses lead to loss of electrical conductivity or complete failure of contacts [17].

Previous studies [18, 19] investigated the effect of pulse laser irradiation $(20 - 25\,\mu s)$ with a large focal spot on metallic mirrors. Using a simple elastic–plastic model of an isotropic material, it was theoretically shown that a surface temperature increase ΔT_y of several tens of degrees generates thermomechanical stresses capable of plastically deforming the mirror surface layer. It was suggested that the accumulated plastic deformation may manifest as slip bands and fatigue cracks, leading to progressive surface degradation [18–20]. But there has been no previous analysis of the role of grain boundaries in such degradation, which is in the focus of our work.

In contrast to microsecond pulses, nanosecond pulses have a much shorter duration, resulting in a shallower heat-affected zone and a more localized thermomechanical response. Plastic deformation of metals under cyclic exposure to nanosecond laser pulses with energies well

* nelasov@icp.ac.ru
† 6asi1z@gmail.com
‡ v-rogalin@mail.ru

below the melting threshold has remained poorly understood. Theoretical studies by Mirzoev, e.g., [21], unfortunately, did not find experimental confirmation at the time. However, in recent years, this phenomenon has been experimentally studied in detail on samples of oxygen-free copper and several of its alloys (Cu–Zr, Cu–Cr, Cu–Zr–Cr, and brass) and reported in dozens of papers (most notably [16, 22–25]), where it was termed the optoplastic effect.

Later studies investigated in detail the most prominent features of this phenomenon, namely the manifestation of grain structure on oxygen-free copper samples [12, 26]. An explanation of this effect was proposed, relating it to cyclic heating and cooling of misoriented grains, and its scope was extended to all cases of localized cyclic thermal exposure not limited to laser pulse heating. These findings are in good agreement with the optoplastic effect observed in our experiments. Accordingly, in this work we refer to this effect as the thermoplastic effect, since the plastic deformation is induced by heating of materials.

The majority of previous studies in this field [1–6, 27] have focused on plastic transformations under shock loading, known as laser shock peening (LSP), whereas all nanosecond (ns) exposures in the ns-LSP regime have amplitudes in the range 1–10 GPa [1–6]. In contrast with this regime the acoustic waves generated in our present work are less than 0.01 GPa. The difference in shockwave pressures by two or more orders of magnitude between LSP and the conditions considered here is due not only to less intense laser heating but also to the use of a liquid layer (usually water) on the surface of workpiece in the ns-LSP method. The formation of residual stresses in LSP requires exceeding the yield strength σ_y of metal. The stress σ_y lies typically within the range of 0.2–0.5 GPa for metals (see Table 2.1 in Ref. [28], as well as in [29]), and it was found that σ_y increases with increasing strain rate [30–33] and with increasing temperature [34].

In all LSP methods, a thin layer is heated to generate sufficiently strong shock waves. The temperature in this layer rises well above the melting temperature, so one typically speaks of a plasma or a plasma layer [1–6, 35–37]. The current classification of LSP methods is as follows:

(A) For sufficiently intense ns exposures, the target is protected (in addition to the liquid) by an additional coating (plastic film or metal foil), which prevents metal evaporation. Absorption of radiation by the coating creates a plasma that, expanding, exerts pressure on the water and the target (see [38] and Sections 4 and 5 in [39]).

(B) For ns pulses that are weaker and somewhat shorter than in regime (A), there is no protective film between water and metal [8, 23, 40]. In this case, the heated layer in the metal acts as a piston and generates a shock wave.

(C) A separate, relatively new branch of LSP is associated with femtosecond exposures: fs-LSP [36, 37, 41, 42]. In this method the generated shock pressures are from hundreds to thousands of GPa [10], which is much higher than 1–10 GPa achieved in ns-LSP. Neither a water overlay nor protective coatings are usually used because such shocks are generated in a very thin heated layer; however, see [43]. Nevertheless, due to the short duration of the triangular-like shock wave (its length is comparable with the heated layer thickness), the depth of hardened layer obtained by fs-LSP is also small. In a quasi-planar propagation regime, the shock wave attenuates with the traveled distance r much more slowly than in the three-dimensional expansion of shock front [44], because the material motion remains quasi-planar as long as r is small compared to the diameter $2R_L$ of the laser spot on the surface. Thus, the large focusing spots are required to make thicker the hardened layer.

In comparison with the above-mentioned plasma-related works, the novelty of our work lies in the theoretical analysis of weak laser exposures, which have remained outside the scope of previous studies, except for the experimental works of the co-authors [16, 23, 25]. Nevertheless, the weak exposures can modify the surface relief and subsurface layer even remaining entirely in the solid phase if the maximal cycle temperature lies below the melting point.

The two main points of this work are as follows.

First, there is the residual thermal expansion of the heated layer in a perpendicular direction (hereinafter referred to as a transverse direction) to the target surface. It is uniform in the longitudinal directions lying in the plane of surface. Under our conditions, the thickness of the heated layer is $\sim 2\,\mu$m (see Section IV), and the residual transverse strain corresponding to layer thickening is a fraction of a percent (see Section V). Consequently, the residual thickening of the layer along the normal to the surface is on the order of 20 nm. This residual transverse deformation is associated with a significant residual tensile stress $\sigma_{res} > 0$ in the longitudinal directions, which is close to the yield strength σ_y.

Second, the experimentally observed nonuniform surface deformations in this work are caused by the different stiffness of adjacent crystal grains (crystallites), which results from the different orientations of their lattices with respect to the target surface. Under sufficiently slow heating, their transverse mechanical stresses in normal to grain boundary direction are identical (but the longitudinal stresses may differ) at their boundary. It leads to different longitudinal deformations of these grains in the target plane, as well as different transverse deformations of the grains (uplift of the free surface) under zero transverse stress. These elastic deformations would be reversible upon cooling of the sample if the arising shear stresses did not exceed the yield strength; however, with further heating, this threshold is overcome. Moreover, the grains of different orientations require different temperature variations (in a range of several hundred degrees), leading to an asynchronous transition of the grains into the plastic regime. Importantly, the stiffness of crystal lattice depends not only on its orientation but also on the defect distribution within it. In particular, the stiffness is strongly reduced near grain boundaries, which leads to large deformations of the target surface along grain boundaries, as shown in this article.

Unfortunately, it is not possible to experimentally detect the residual thermoplastic deformations/stresses on crystallite surface areas away from grain boundaries; these deformations/stresses belong to the first point above (the homogeneous region approximation). Such an approximation is applicable because the grain size of $40-50\,\mu$m is much larger than the thickness of the heated layer $1.5-2\,\mu$m. Therefore, the experimental part of our work mainly concerns surface modifications along the grain boundaries.

The key concept in elastic–plastic theories is the yield strength σ_y of material. Since the shockwave pressures are lesser than 10 MPa in our work, the deformation of crystallites is determined by stresses produced by thermal expansion/contraction. Those thermomechanical stresses may reach 200–500 MPa, which are comparable to σ_y of copper.

The thermomechanical stresses in a plane layer of finite thickness is proportional to the temperature variations during heating/cooling for elastic deformations. Under such conditions, it is convenient to use the temperature increase ΔT_y required for the shear stresses to overcome the yield strength. Such ΔT_y is proportional to the ratio of σ_y to a characteristic stiffness C of material, which is determined by elastic constants combination depending on the direction of crystal deformation. For an isotropic solid, C is a combination of the bulk and shear moduli – see Eq. (8) in Section VI. Also ΔT_y is inversely proportional to the coefficient of thermal expansion α (see Appendix for its definition and numerical value), because the quantities $\alpha\Delta T_y$ and σ_y/C should be comparable.

The work [45] is relevant to our study, since it uses continuum modeling of a thin layer of many misoriented deformable grains. However, the grain boundary movement occurs only through grain deformation, so the grains cannot change their masses. Also, twinning is not considered in the hardening models in Ref. [45]. In contrast to this, our experiments involve a bulk copper sample with crystallite sizes of about $40\,\mu$m comparable to the laser spot size of about $100\,\mu$m, so only a few grains are exposed. Whereas in [45] a purely mechanical loading (without heating/cooling) produces the transverse tensile and compressive strains similar to ultrasonic action, in our work the thermomechanical stresses arising from weak but thermomechanically significant nanosecond heating are responsible for deformation. To shed light on atomistic processes underlying the plastic behavior of materials under thermocycling we also performed large-scale molecular dynamics (MD) simulations (Section VII), which allow observation of actual processes of grain growth, shrinkage, and even disappearance, occurring mainly through grain boundary migration.

The paper first presents the experimental methods and results in Sections II and III. The following four sections describe the simple theory, continuum modeling and MD simulations.

The theoretical part begins with Section IV, which presents 1D continuum modeling of purely elastic copper under laser heating up to the melting temperature. Solution of the thermal problem, including a shock-acoustic effect, is obtained there. It is demonstrated that the calculated acoustic stresses are well below the yield strength, and plasticity can be governed only by thermal stresses in contrast to the ns-LSP regime, in which plastic phenomena are driven by shock loading. In our conditions the heated material moves with velocity much smaller than the sound speed. Thus, the problem can be treated by an elastostatic approach.

Elastostatics regime is considered in Section VI, where a plane single-crystal slab is subjected to uniform thermal expansion. Due to the free condition at the slab surface the corresponding transverse stress $\sigma_{zz}=0$, It is shown that the longitudinal stresses σ_{xx},σ_{yy} in plane of the slab and transverse deformation u_{zz} strongly depend on the orientation of crystal, and the yield stress in copper can be achieved by temperature rise of several hundreds degrees as our experiment. But in polycrystalline materials with grain crystal lattices orientating arbitrary the in-plane longitudinal deformations of adjacent grains are not necessarily zero (though their net transverse deformation is zero). From the continuum mechanics standpoint, the neighbor grains in a polycrystalline layer must stay in mechanical equilibrium, if heating is slow enough. Because of the orientation dependence of stiffness (for example, for cubic crystal, the stiffness in the [100] direction is the elastic constant $C=c_{11}$, while in the [110] direction it is $C=(c_{11}+c_{12}+2c_{44})/2)$, such equilibrium can only be achieved with significantly different deformations of the grains both in the longitudinal directions and in the transverse direction perpendicular to the surface. Since the lattice stiffness depends strongly on the defect distribution, the local stiffness (and also the local yield strength) is reduced near grain boundaries, where they intersect the free surface, leading to large deformations of the heated surface along those grain boundaries.

The plastic deformation of an isotropic solid slab with two free boundaries is modeled in Section V using a simple elastic–plastic model. Three deformation regimes of the slab heated by consecutive laser pulses are described. In the first regime, the layer remains elastic. No residual deformations or stresses remain after cooling to the initial temperature. In the second regime, the yield strength σ_y is reached during the heating stage. The solid reaches its yield strength at a certain temperature rise, which is $\Delta T_y=159$ K for the given $\sigma_y=500$ MPa of copper. However, during the cooling stage in this regime, the system does not reach σ_y. The calculation shows a transition from the initial stress-free state to a stressed state in which the system behaves elastically under repeated laser pulses of the same intensity.

In the third regime, the thermal action of the laser is sufficient to exceed the threshold σ_y both during heating and cooling. It is found that the system follows a closed loop that repeats upon subsequent laser pulses in the strain–stress plane $u-\sigma$. Such loops in the stress–strain plane are well known in elastic–plastic models of solids (see, e.g., Figs. 6–8 in [45] or Fig. 2.1 in [28]). But in our work the similar thermomechanical loops occur if the yield strength is reached at a temperature rise ΔT_y rather than at a certain strain increment.

Reaching the loop implies saturation of the growth of residual deformations and stresses under repeated laser exposures, analogous to the saturation shown in Fig. 15 of [45] for mechanical tension–compression. However, in our experiments, the amplitude of the surface deformations near the grain boundaries increases with the number of exposures. This issue requires further theoretical investigation, because Sections IV–VII deal with situations of a homogeneous layer and/or uniform heating. Future work should extend these to the case of two adjacent crystallites with a high-angle interface.

Section VII presents the results of MD simulations of a polycrystalline slab. This atomistic method lets us observe twinning and grain boundary migration between interacting crystal grains under spatially uniform slow heating, which generates the identical normal stresses between adjacent grains. The MD simulations revealed the asynchronous response of misoriented grains to loading, due to their different stiffnesses. This led to anisotropy of grain deformation, as well as an increase in the surface height difference after each heating–cooling cycle.

II. MATERIALS AND METHODS

The material selected for this study was oxygen-free copper with a purity of 99.999 % and a face-centered cubic (FCC) lattice. Experimental samples were machined from this material into disks 40 mm in diameter and 10 mm thick. The surface of the initial sample was ground and then polished to the roughness of approximately 15–20 nm over an area comparable to the laser spot size. Chemical–mechanical polishing ensured reproducible initial conditions and eliminated any influence of the original topography on the measurement results [46]. The laser irradiation conditions and procedures were identical to those used in previous studies [16, 22]. The samples were exposed to a nanosecond Nd:YAG laser system operating at the third harmonic (wavelength $\lambda = 355$ nm, pulse duration (FWHM) $\tau = 10$ ns, pulse repetition frequency $f = 10$ Hz). The spatial beam profile corresponded to a Gaussian distribution (TEM_{00} mode). The radiation was linearly polarized and focused onto the polished sample surface using a quartz lens. All experiments were performed in air under ambient conditions. The fluence was varied in the range $F \approx 0.6 \ldots 1.05$ J/cm^2.

The present work focuses not only on low-fluence regimes (up to 1.05 J/cm^2) but also on the investigation of pre-melting processes that occur in the condensed state of the material. The time interval between pulses was 0.1 s, which ensured complete cooling of the surface be-

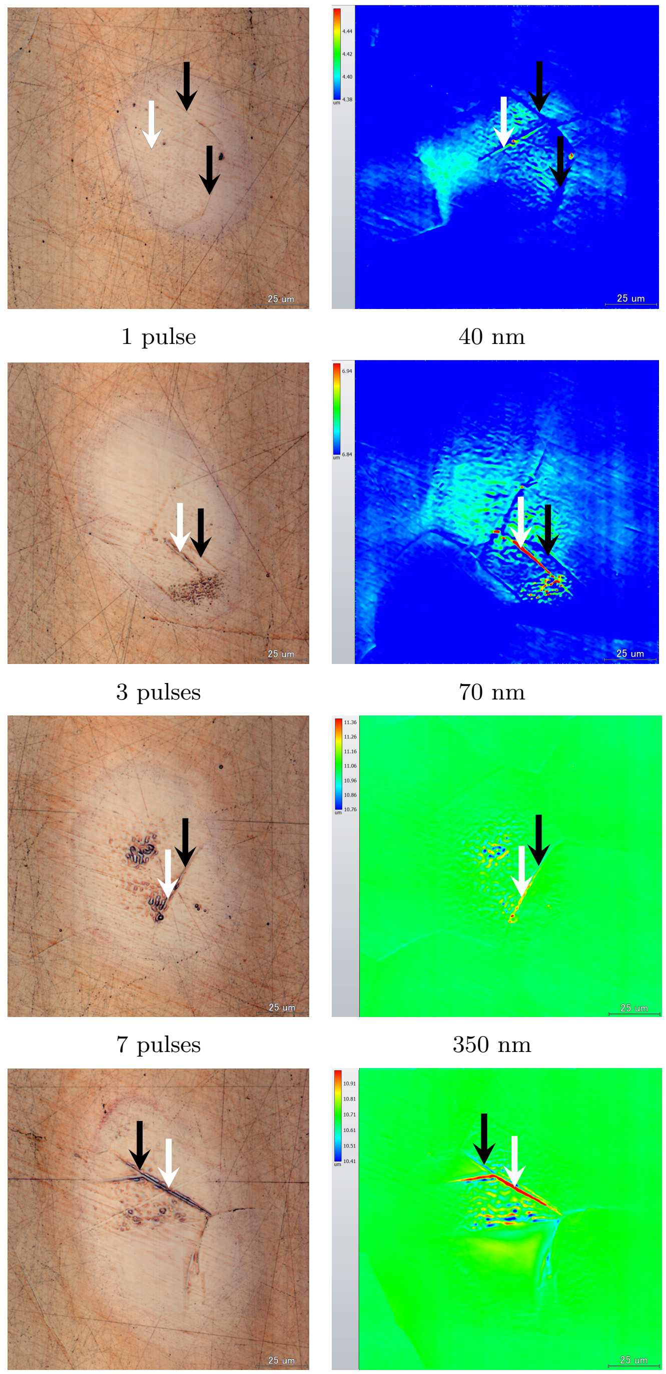

1 pulse | 40 nm
3 pulses | 70 nm
7 pulses | 350 nm
15 pulses | 500 nm

FIG. 1: Confocal scanning laser microscopy of the oxygen-free copper surface after exposure to nanosecond UV laser pulses (355 nm, 10 ns, $F = 1.05$ J/cm^2). Micrographs (left) and pseudo-colored relief maps (right) are shown for $N = 1$, 3, 7, and 15 pulses, with the maximum height variation of relief nearby the grain boundary indicated in nm. Arrows on micrographs and relief maps point to the same surface features near grain boundaries; dark arrows indicate depressions, light arrows – protrusions.

fore the next pulse arrived. A characteristic pre-ablation regime was thus realized, in which protrusions and depressions formed near grain boundaries ($F = 0.6{-}1.05$ J/cm^2, $N = 1{-}15$) were observed, as previously reported in [12, 26].

Confocal scanning laser microscopy was performed using an Optelics Hybrid LaserTec instrument, following the same protocol as in previous work [12]. This method provided three-dimensional surface topography maps with a vertical resolution down to a few nanometers. For each set of parameters (F, N), 3D profilograms were constructed, which served to validate the continuum model (Fig. 1). Detailed morphological analysis of the laser-exposed surfaces was carried out by scanning electron microscopy (SEM) using an FEI Scios DualBeam instrument (SRC "Crystallography and Photonics" RAS). Observations were performed in secondary electron (SE) mode with an Everhart–Thornley detector (ETD) at an accelerating voltage of 5–10 kV and a probe current of 0.4–6.4 nA. SEM imaging revealed submicron surface features (slip steps, micro-protrusions, regions of local material extrusion) that were not accessible by confocal microscopy. It also confirmed the absence of intense ablation indicators, such as frozen melt droplets or spatter traces.

To investigate the changes in microstructure of the copper surface layer of a few hundred nanometers thick, the transmission electron microscopy (TEM/STEM) was performed using a Tecnai Osiris microscope operated at an accelerating voltage of 200 kV. Thin lamellae (80–100 nm thick) were cut perpendicular to the irradiated surface from characteristic regions of the laser spots by focused ion beam (FIB) thinning using the FEI Scios DualBeam instrument, following the procedure detailed in [47]. Bright-field and dark-field TEM images were recorded to visualize dislocation structures, deformation twin packets, and low-angle boundaries. Selected area electron diffraction (SAED) patterns were also acquired, allowing analysis of the matrix crystallographic orientation, identification of twin orientations, and estimation of subgrain misorientation angles. The chemical composition of the surface layer was characterized by energy-dispersive X-ray spectroscopy (EDX) using the STEM Tecnai Osiris system. EDX mapping confirmed that copper remained the main component of the near-surface layer under all investigated exposure regimes. No significant chemical modifications (oxide phases, impurity segregations) that could substantially affect the mechanical properties of the layer were detected.

For the theoretical description of the observed phenomena, a continuum thermomechanical elastic–plastic model was developed and implemented in a Lagrangian formulation with finite-difference approximation. The laser heating profile was described by a Gaussian function corresponding to the TEM_{00} mode of the laser used.

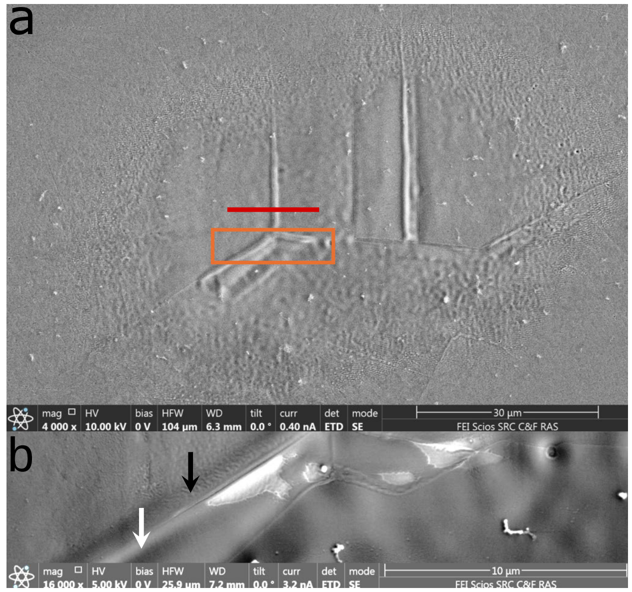

FIG. 2: Scanning electron microscopy of the copper surface after laser exposure. **(a)** Overview image of the laser spot region, where the red line marks the lamella cutting region and the rectangle indicates the area shown at higher magnification in **(b)**. There are dark arrows indicating depressions at the grain boundary, and light arrows indicating protrusions.

III. EXPERIMENTAL RESULTS

At the pulse repetition rate of 10 Hz used in this work, each subsequent laser pulse irradiates the metal surface (oxygen-free copper) only after the target has completely cooled from the previous pulse. During the experiment, a gradual transformation of the laser spot was observed, depending on the fluence F and the number of consecutive pulses N. A thermoplastic effect, previously reported in [16, 22], was observed during the early exposure stages. Figure 1 presents surface images (left column) alongside profilograms obtained by confocal scanning laser microscopy (right column) for several laser spots on the oxygen-free copper samples. This figure illustrates the evolution of the surface changes after exposure to nanosecond UV laser pulses as the number of pulses increases from 1 to 15. The cumulative nature of relief formation is clearly visible with increasing pulse count.

Confocal scanning laser microscopy revealed that, under repeated cyclic laser exposure, depressions and protrusions form near the grain boundaries of the original grain structure (Fig. 1) – see, for example, the surface state after 15 pulses. These changes occur within the fluence range of 0.6 to 1.05 J/cm^2, and their appearance depends on both the fluence and the number of pulses. The height difference between the corresponding protrusion and depression localized nearby the grain boundary increases with the number of pulses and reaches about

500 nm after 15 pulses.

During subsequent cooling, the material does not return to its initial state because of accumulated irreversible plastic deformation. The pronounced height differences near grain boundaries confirm that the primary relief formation mechanism is thermoplastic extrusion rather than material ablation (evaporation). Thus, the formation and growth of the relief are driven by the relaxation of thermoelastic stresses during cyclic heating and cooling.

Scanning electron microscopy (SEM) provided detailed insight into the laser spot morphology, revealing characteristic relief features (Fig. 2a) not accessible by confocal microscopy. Overview images clearly show the overall structure of the laser-affected zone: a central region with protrusions and depressions, and a peripheral region largely devoid of signs of intense ablation. No significant solidified melt droplets or splashing are observed at the periphery, confirming the dominant role of the thermoplastic deformation mechanism. At the highest magnifications, submicron relief details become apparent, including slip steps, micro-protrusions, and regions of local material extrusion (Fig. 2b).

To elucidate the nature of structural changes in the thin surface layer, TEM lamellae were prepared perpendicular to the surface from selected regions of the laser spots using focused ion beam (FIB) milling. Bright-field and dark-field TEM images of the surface layer formed under the pre-ablation regime revealed characteristic signs of developed plastic deformation: nanoscale deformation twin plates in individual grains, previously observed in [12] (Fig. 3b,c), as well as the well-developed dislocation substructures and zones with a high density of deformation defects in the grain boundary regions. These features are particularly pronounced in the surface layer, which is 200–500 nm thick.

In scanning transmission electron microscopy (STEM) mode, overview images reveal the defect density of the surface layer. The concentration of structural defects is highest in a layer several hundred nanometers thick directly beneath the material surface (Fig. 3a,b). This distribution of structural damage is consistent with the calculated strain profile from continuum modeling, where maximum plastic strain is also concentrated near the irradiated surface. Deformation twinning and the formation of dislocation substructures occur simultaneously within a single thermomechanical heating–cooling cycle. This indicates that the temperature in the surface layer during exposure significantly exceeded the activation threshold for high-temperature dislocation glide and climb (≈ 0.4–$0.5T_\mathrm{m}$), without reaching the melting temperature.

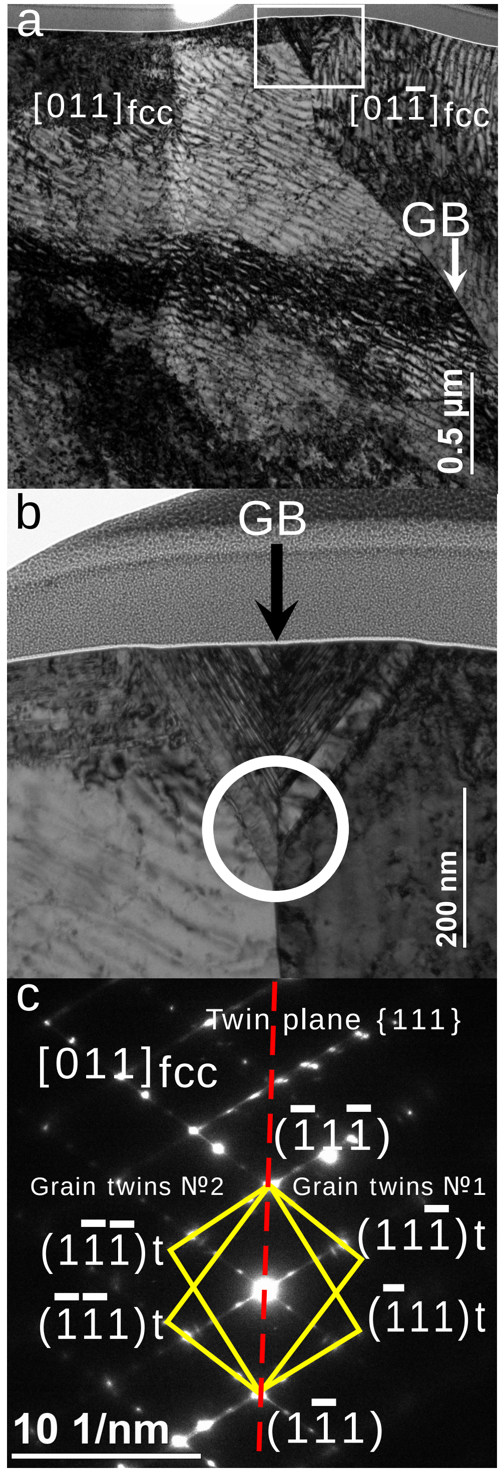

FIG. 3: Transmission electron microscopy of lamella taken from place shown in Fig. 2. GB indicates a grain boundary. **(a)** – the bright-field overview image of lamella with white rectangle region showing nanoscale deformation twin plates. **(b)** – the enlarged rectangle with GB. **(c)** – diffraction pattern from a white circle in (b), zone axis $\langle 011 \rangle$.

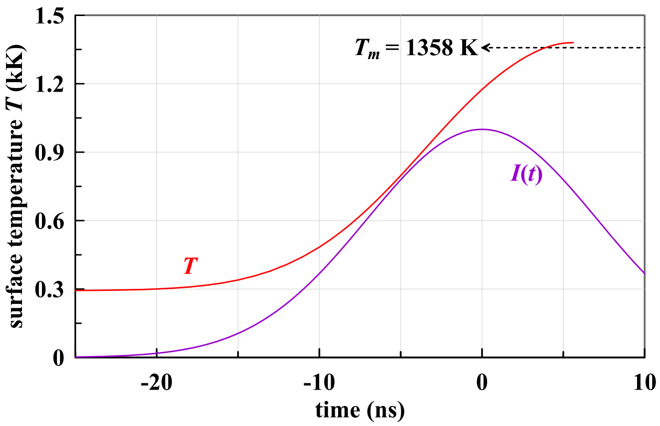

FIG. 4: Surface temperature evolution (red curve) due to heating by a laser pulse of duration $\tau_L = 10\,\text{ns}$. For comparison, the normalized intensity $I(t) \sim \exp(-t^2/\tau_L^2)$ is shown by the violet curve. The temperature maximum is shifted relative to the intensity maximum because the surface temperature is determined by the balance between the laser energy delivered into the target skin layer and the heat flux conducted from the skin layer into the bulk of the target. Initially, energy input dominates, followed by heat removal.

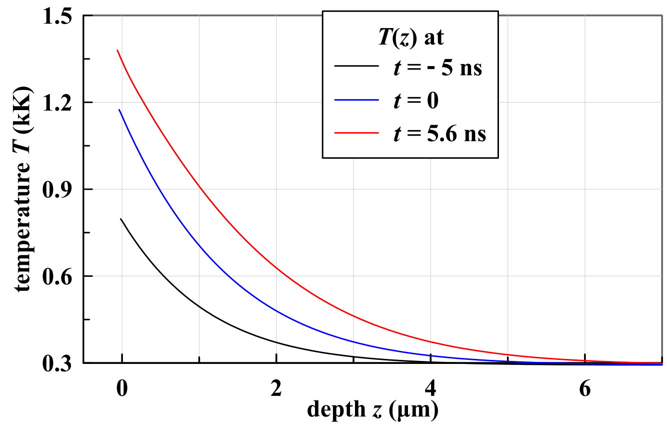

FIG. 5: Temperature profiles in depth of copper at several times. The time $t = 0$ corresponds to the maximum of laser intensity. The slight leftward shift of profiles is caused by thermal expansion of material.

IV. HYDROCODE MODELING OF ELASTIC SOLID HEATED BY A LASER PULSE

Our in-house two-temperature one-dimensional hydrocode 2T-HD is used for modeling of elastic solid. Since the laser spot diameter is $100 - 150\,\mu\text{m}$ while the heat penetration depth is only about $2\,\mu\text{m}$, the lateral temperature gradients are negligible, which allows us to employ the one-dimensional approach. This code is universal and applicable to a wide range of problems in laser–matter interaction for various pulse durations and absorbed fluences, including femtosecond laser heating [48–50]. It was also utilized for modeling of nanosecond pulses [8, 39], for which the electron and lattice temperatures are virtually identical.

Figures 4–8 show the main results of the 2T-HD modeling. The laser intensity $I(t)$ absorbed within a skin layer of copper is approximated by a Gaussian function with the pulse duration $\tau_L = 10\,\text{ns}$, see the violet curve in Fig. 4. The source is normalized such that the absorbed fluence

$$F_{abs} = \int_{-\infty}^{\infty} I(t)dt$$

equals $0.75\,\text{J/cm}^2$. The modeling starts at $t = -3\tau_L$, when the laser intensity is negligibly small. The copper parameters used in modeling are presented in Appendix.

The surface temperature reaches its maximum at $t \approx 5.6\,\text{ns}$ and then begins to decrease (see red curve in Fig. 4). Since the used $F_{abs} = 0.75\,\text{J/cm}^2$ is only about 1.2% above the melting threshold, the maximal surface temperature exceeds the melting point by 16 degrees only. Such overheating does not affect the modeling results since the melting process is excluded from modeling. The radiative loss rate is too slow for the surface at this relatively low temperature and it is neglected in our modeling.

In real conditions, the laser radiation is absorbed in a skin layer with the thickness of 10 nm, which is very small compared to the heated layer thickness, which is about $2\,\mu\text{m}$ for a nanosecond pulse. The thermal conduction of absorbed laser energy allows us to replace the direct modeling of such localized absorption by a simple boundary condition of an energy influx $I = -\kappa dT/dz$ through the free surface, where κ is a heat conduction coefficient. This is why the profiles $T(z)$ shown in Fig. 5 for the three times have a finite slope near the surface.

Figure 6 demonstrates that the calculated transverse stresses P_{zz} are much lower than pressures generated by a similar absorbed fluence used in Refs. [8, 39], where the metal target was covered by a water layer and the laser pulse had the shorter duration of 0.5 ns. It led to the recoil pressure much higher for similar heating temperatures. Thus, if expansion occurs into air, the pressure in the target can be much lower compared to expansion into water. The demonstrated here regime with such low transverse stress P_{zz} has apparently not been considered previously.

Note that because the amplitude of the acoustic wave is extremely small, the nonlinear effects are absent in our conditions. That is, a simple Riemann wave does not steepen and does not overturn to form a shock wave.

There are many studies of reactive recoil due to a plasma plume. At lower intensities, the pressure in the target is generated by vapor outflow. In this study the momentum compensation (the photon momentum is neglected) occurs via expansion of the heated solid part of the target toward the incident laser beam. Vapor recoil

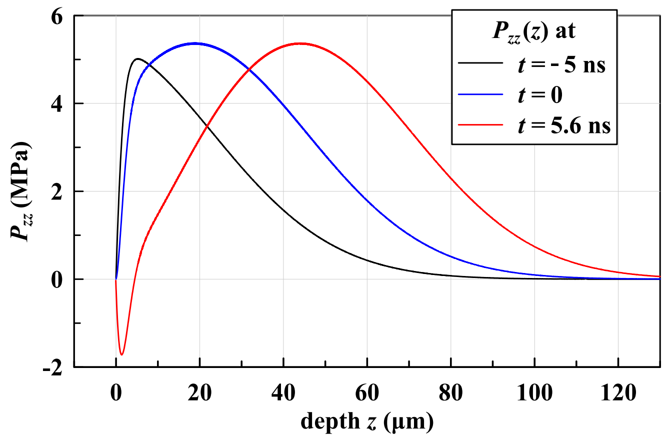

FIG. 6: Distribution of the transverse stress P_{zz} with depth z measured from the initial position of the free surface. The calculation stops shortly after the appearance of a small region of tensile stress near the free surface soon after the heating intensity starts to decrease. As can be seen, the acoustic wave emitted into the bulk has a small amplitude.

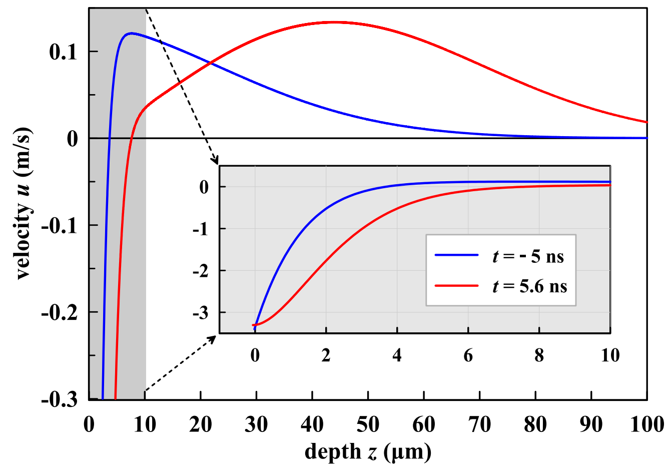

FIG. 7: The material flow velocity $u \sim 0.1\,\mathrm{m/s}$ produced by the acoustic wave is much smaller than the thermal expansion velocity (several m/s), which is localized in a narrow heated layer of several micrometers thick nearby the free surface (shown in the gray inset). Note that due to deceleration by the tensile stress in Fig. 6, the surface velocity becomes smaller with time.

momentum can be also neglected because the saturated pressure $6 \cdot 10^{-8}$ MPa of copper vapor is very small at the melting temperature. Consequently, the momentum of the acoustic motion to the right in Fig. 6 is almost exactly opposite to the momentum of the heated solid copper layer expanding to the left. This situation is illustrated in Fig. 7. Note that the displacement of the free surface over the time interval shown in Fig. 7 is about 70 nm.

The first characteristic starts at the beginning of modeling at $-3\tau_L$ and propagates into the bulk of target to the depth of $170\,\mu$m, but its amplitude is vanishingly small. Taking the position of pressure maximum $43\,\mu$m in Fig. 6 at $t = 5.6$ns, which coincides with the velocity maximum in Fig. 7 at the same time, and dividing by the longitudinal sound speed, one can obtain 9 ns. That is, the characteristic corresponding to the maximum leaves a region near the free surface 9 ns prior to $t = 5.6$ns. Thus, this characteristic was emitted at $t = -3.4$ns in the used time axis.

This version of the 2T-HD code operates within the framework of linear elasticity. Let us introduce the normal (diagonal) components of the stress tensor σ_{ik} with the transverse component σ_{zz} and the longitudinal components σ_{xx}, σ_{yy} in plane of the target surface. For the isotropic elastic solid $\sigma_{xx} = \sigma_{yy}$ everywhere in an infinite plane layer.

Figure 6 shows the component P_{zz}, which by definition is $P_{ik} = -\sigma_{ik}$. Stress and deviatoric stress are related to the hydrostatic pressure as follows

$$P_{zz} = P - s_{zz}, \tag{1}$$

Figure 8 shows distributions of the transverse deviator s_{zz} and the pressure P obtained in modeling. The last is calculated from the local density and temperature using the equation of state. Having pressure and deviator the stress is calculated using Eq. (1).

Comparison of pressure, stress, and deviator presented in Eq. (1) can be done by examining Figs. 6 and 8. It is seen that the two terms on the right-hand side of Eq. (1) compensate each other to within a fraction of a percent. Thus, the situation is described with high accuracy in the elastostatic approximation. This is due to the slow heating:

$$\tau_L \gg t_s, \quad t_s = d_T/c_s. \tag{2}$$

Here $\tau_L = 10$ns is the duration of the nanosecond pulse, $t_s = 0.5$ ns is the acoustic time scale, $d_T \sim 2\,\mu$m is the heated layer thickness (see Fig. 5), and c_s is the sound speed. In the elastostatic approximation, the kinetic energy is small, and the thermal expansion and the associated decrease in hydrostatic pressure are compensated by elastic forces.

In the following two sections, the problem is analyzed in the elastostatic approximation because of condition (2), i.e., inertial-acoustic effects can be neglected. Section VI treats the elastic thermal expansion of a single-crystal layer with one or two free boundaries. It will be shown that, unlike an isotropic solid, the thermal stresses strongly depend on the orientation of the single-crystal lattice relative to the layer surface.

For an infinite plane layer heated uniformly, the problem with two free boundaries can be reduced to a problem with one free boundary and a contact with a cold half-space solid. Thus, the solid heated layer is tightly bonded to the underlying cold solid. A uniform one-dimensional approximation (only one spatial variable

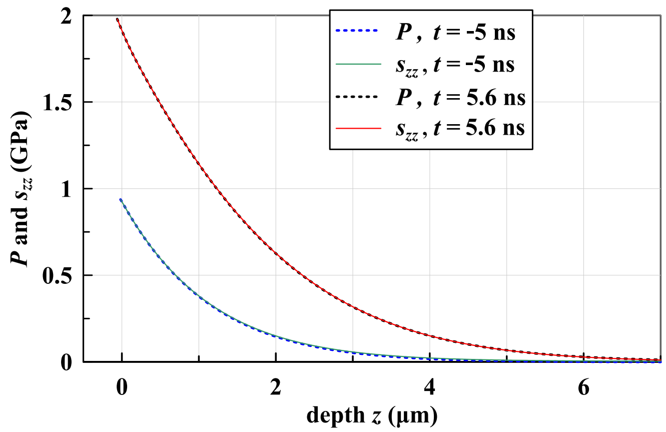

FIG. 8: Hydrostatic pressures P (dashed curves) and deviators s_{zz} according Eq. (1) (solid curves) are nearly coincide on the figure scale. Their difference is the stress P_{zz}, which is two to three orders of magnitude smaller in amplitude (cf. Figs. 6 and 8). The deviator exceeds the yield strength.

z is free) can be used in such conditions. Indeed, the longitudinal deformations are not allowed, and the hot layer expands into the cold half-space while satisfying the force and kinematic boundary conditions at the interface. Such formulation exactly corresponds to the sample modeled in this Section.

To model the exceeding of yield strength, the problem is solved in an elastic–plastic formulation in next Section V. Since the laser spot contains only a few crystallites, it is important that the calculations in Section V are performed in the homogeneous one-dimensional approximation. Except for the small areas of grain boundaries, where the uniform one-dimensional approximation is not applicable, this 1D approximation is applicable for most of the spot area.

V. ELASTIC-PLASTIC MODELING OF A PLATE SUBJECTED TO THERMOCYCLING

To simulate the cyclic thermal loading of a metal sample subjected to repetitive nanosecond laser pulses, a Lagrangian grid method is used to solve the transport equations for mass, momentum, and energy in a deformable material [51]. Laser heating is accounted for by adding a power source $\dot{Q}(\vec{r},t)$ (absorbed energy per unit mass per unit time) to the energy balance. Under the experimental conditions, the metal rapidly cools between laser pulses due to heat conduction into the bulk of the sample; therefore, in our simplified model, $\dot{Q}(t)$ acts alternately as a heating term during the pulse and as a cooling term between pulses, thereby representing both heating and cooling.

To close the system of balance equations, material models are employed: an equation of state $P = P(\rho, e)$ describing the dependence of hydrostatic pressure on density ρ and specific internal energy e, and an elastic–plastic model defining the relationship between strain and the stress tensor. In this work, the Mie–Grüneisen equation of state for copper is used to compute the hydrostatic pressure:

$$P = P(\rho, e) = P_r(\rho) + \rho\Gamma(e - e_r(\rho)) \tag{3}$$

with reference curves $P_r(\rho)$ and $e_r(\rho)$ determined from the shock adiabat $u_s = c_0 + su_p$, where u_s is the shock-wave speed, u_p is the particle velocity, and the linear coefficient $s = 1.495$ is adopted for copper. The reference curves with the material parameters and the elastic–plastic model for copper are presented in Appendix.

Uniform thermocycling of a plate

Formation of plastic strains and stresses arising from spatially uniform thermal cycling of a copper sample is studied here. As shown in the previous section, the temperature increase of a few hundred degrees is sufficient to produce the plastic deformation of material remaining in a solid state.

Consider an infinite copper plate (layer) of small thickness in vacuum. We define the coordinate system: X and Y are in-plane (longitudinal) directions parallel to the target surface, and Z is the normal (transverse) direction perpendicular to the surface. Hereafter, "longitudinal" refers to directions in the plane of the surface, and "transverse" refers to the direction normal to the surface. The layer is bounded by two free surfaces at $Z =$constant. In the calculation, a square piece of the plate is used with periodic boundary conditions on the longitudinal axes (X, Y).

Spatially uniform heating–cooling cycling causes deformation of such a plate only in the vertical direction along $Z-$axis. Such assumption is applicable to the experimental deformation of a sufficiently thin plate heated by a laser pulse with both the diameter of focal spot and the heating depth much larger than the plate thickness.

Consider a relatively low thermal load where the sample undergoes only elastic reversible deformations. For this purpose, the sample is heated by a heat source $\dot{Q} = 1.2 \cdot 10^9$ J/kg/s for $\Delta t = 50\,\mu s$. The absorbed specific energy per heating cycle is then $\dot{Q}\Delta t = 0.06$ MJ/kg. Under these conditions, the rate of energy deposition is low. Consequently, the strain rate is small, and mechanical equilibrium is reached without the generation of noticeable acoustic waves, as described above in Section IV. Nevertheless, to allow any weak waves to decay and full mechanical equilibrium to be established, the copper sample is left at rest for $\Delta t = 50\,\mu s$ after the heating stops.

The sample is then cooled back to its initial internal energy at the same rate $\dot{Q} = -1.2 \cdot 10^9$ W/kg. Figure 9(a) shows the evolution of the longitudinal stress

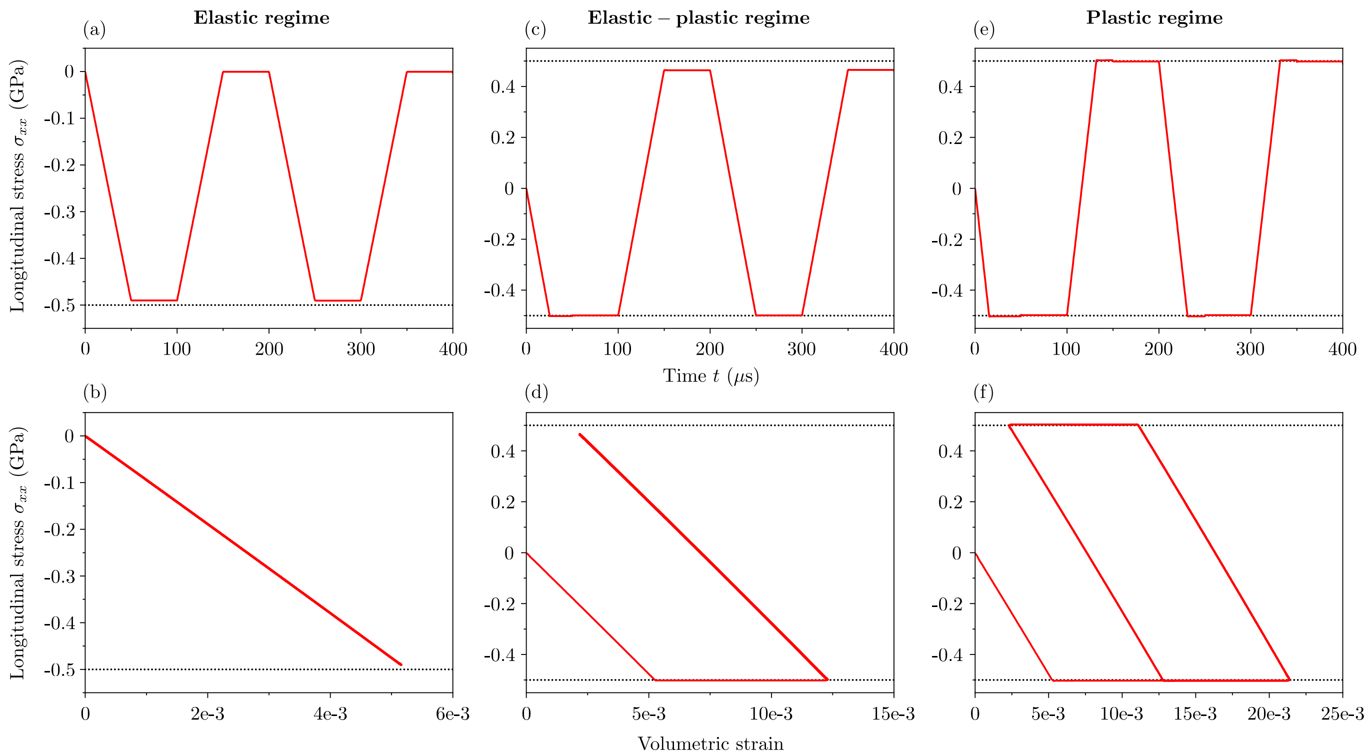

FIG. 9: Uniform thermocycling of a copper sample at various heating powers: 1) elastic deformation regime with $\dot{Q} = 1.2\,\mathrm{GW/kg}$ and total deposited energy $Q = \dot{Q}\Delta t = 0.06\,\mathrm{MJ/kg}$ (a,b); 2) transitional elastic–plastic regime with $\dot{Q} = 2.4\,\mathrm{GW/kg}$ and $Q = 0.12\,\mathrm{MJ/kg}$ (c,d); and 3) plastic regime with $\dot{Q} = 4\,\mathrm{GW/kg}$ and $Q = 0.2\,\mathrm{MJ/kg}$ (e,f). Panels (a,c,e) show the different longitudinal stresses $\sigma_{xx}(t)$ generated in various regimes; panels (b,d,f) show the σ_{xx} as functions of the volumetric strain $\mu = 1 - \rho/\rho_0$. The dashed lines indicate the stress level at which the plastic regime is activated by the von Mises criterion described in Appendix.

σ_{xx} (parallel to the free surface) for this thermal loading regime. It can be seen that during the heating stage $t \in [0, 50]\,\mu$s, σ_{xx} increases linearly with time without reaching the yield strength, indicating purely elastic deformation. During the cooling stage $t \in [100, 150]\,\mu$s, σ_{xx} also decreases linearly to zero, returning to its initial state.

The transverse stress to the free surface remains essentially zero, $\sigma_{zz} \approx 0$, as expected for sufficiently slow thermal cycling. Subsequent heating–cooling cycles proceed in the same manner without irreversible plastic deformation. In this purely elastic regime, the states of system lie on a straight line in the σ_{xx} vs. volumetric strain $\mu = 1 - \rho/\rho_0$ plot, as shown in Fig. 9(b).

With increasing deposited energy, the equivalent shear stress also increases, which will cause plastic deformation if the yield strength σ_y is exceeded. To investigate this regime, a heat source $\dot{Q} = 2.4 \cdot 10^9$ J/kg/s is used for $\Delta t = 50\,\mu$s. The specific energy per heating cycle is then $\dot{Q}\Delta t = 0.12\,\mathrm{MJ/kg}$, twice that of the previous purely elastic regime.

Figure 9(c) shows that the internal stresses reach the critical value at approximately $25\,\mu$s and then cease to increase despite continued heating, indicating the onset of plastic deformation. It can also be seen in Fig. 9(d) that the elastic stage lasts until the volumetric strain reaches $\mu \simeq 0.005$, after which the sample deforms plastically.

A characteristic feature of this elastic–plastic regime is that during cooling, the stress is proportional to strain, and no plastic deformation occurs, in contrast to the initial heating stage. This behavior arises because during cooling the sample unloads from a pre-stressed state, allowing it to deform elastically over a larger strain range compared to starting from its original stress-free state. Thus, after a complete cycle, residual in-plane stress and volumetric deformation remain in the sample, as clearly seen in the plots.

It should be noted that in the second and subsequent heating–cooling cycles, the sample deforms only elastically, because each stage begins not from the virgin state but from a pre-stressed one.

When the deposited energy is even larger, plastic deformation occurs both during heating and during cooling, and this behavior repeats in all thermal cycles. In this third regime of thermal loading, a heat source $\dot{Q} = 4 \cdot 10^9\,\mathrm{W/kg}$ is used for $\Delta t = 50\,\mu$s. The absorbed specific energy per heating cycle is $0.2\,\mathrm{MJ/kg}$. The transverse stress remains $\sigma_{zz} \approx 0$.

The evolution of the in-plane longitudinal stress σ_{xx} in Fig. 9(e) shows that the heating stage of the first cycle resembles the previous elastic–plastic regime. However, the transition from elastic to plastic behavior occurs earlier because the heating intensity is higher.

The main difference appears during the cooling stage: now the deformation is sufficiently large that plastic flow occurs not only during heating but also during cooling, as clearly seen in Fig. 9(f): after a linear elastic segment, a plastic deformation segment follows, characterized by constant stress.

In the second cycle, the heating stage starts from a pre-stressed state: first the sample deforms elastically (linear increase of stress), then plastically (segment with constant stress), and eventually the final state coincides with the state after the heating stage of the first cycle. Therefore, the cooling stage in the second cycle (and in all subsequent cycles) replicates the cooling stage of the first cycle. Thus, the stress–strain curve forms a hysteresis loop in this regime, as shown in Fig. 9(f).

Within the proposed simplified model, further increase of the deposited energy does not change the qualitative picture described above. Increasing the number of heating–cooling cycles also does not lead to any changes. In reality, the loading picture would be somewhat more complicated because real materials are not ideal elastic–plastic bodies with a fixed yield strength. In particular, fatigue failure may occur with a very large number of loading cycles. Using more adequate material models with a history-dependent yield strength could potentially reproduce such failure, but this is beyond the scope of the present study.

Temperature variation leading to yield

The simple numerical solutions obtained above can be represented by analytical formulas. To derive such solution, the following equation for thermomechanical stresses [52] is used

$$\sigma_{ik} = -\alpha K \Delta T \delta_{ik} + K \delta_{ik} u_{ll} + 2G(u_{ik} - \delta_{ik} u_{ll}/3), \quad (4)$$

where summation over repeated indices is implied, and ΔT is the temperature variation. The used parameters K, G, and α are the isothermal bulk modulus, shear modulus, and volumetric thermal expansion coefficient, respectively – see the corresponding values in Appendix. This equation follows from the expression for the free energy of elastically deformed solid [52], see also [53].

In accordance with the uniform heating of the layer, Eq. (4) can be written in the principal axes, where the tangential components of stress tensor vanish. The longitudinal strains set zero: $u_{xx} = u_{yy} = 0$. Neglecting inertia and taking into account the free boundary conditions on the top and bottom surfaces we obtain $\sigma_{zz} = 0$ throughout the layer. Finally the expressions for the in-plane stress σ_{xx} and the transverse strain u_{zz} in the purely elastic regime are:

$$\sigma_{xx} = -2\alpha \Delta T G/[1 + 4G/(3K)], \quad (5)$$

$$u_{zz} = \alpha \Delta T/[1 + 4G/(3K)]. \quad (6)$$

For an ideal elastic–plastic solid with the fixed yield strength σ_y, the von Mises equivalent stress is assumed to be $\sigma_e = \sigma_y$ in the plastic regime, which gives $\sigma_{xx} = \sigma_e = \sigma_y$ according to Eq.(17) and

$$u_{zz} = \alpha \Delta T. \quad (7)$$

Equations (5-7) are in good agreement with the modeling results in Subsection V, despite some difference in the used equation of states, see Eqs.(3,A1).

The stress given by Eq. (5) increases with temperature, and the transition from elastic to plastic deformation occurs when the longitudinal stress σ_{xx} reaches the σ_y. Equating the stress from Eq. (5) to the yield stress gives the temperature variation ΔT_y required to initiate plastic deformation:

$$\Delta T_y = \frac{\sigma_y}{2\alpha G}\left(1 + \frac{4}{3}\frac{G}{K}\right). \quad (8)$$

Substituting the parameters for copper into Eq. (8) provides the temperature variation $\Delta T_y = 159\,\mathrm{K}$ to reach the yield strength in an initially unstressed layer. The corresponding increase in energy density is $C_p \Delta T_y \approx 61\,\mathrm{J/g}$.

The yield strength can be also reached for a prestressed layer with some residual stress remaining after cooling. But the twice higher temperature variation is required $\Delta T_{y2} = 2\Delta T_y$ than in the first heating, which gives $\Delta T_{y2} = 318\,\mathrm{K}$ for copper. The reason for such doubling is that the material reaches the radius of the Mises cylinder from the unstressed state in the first heating, while in subsequent cycles it is necessary to cross the Mises cylinder in diameter to attain again the yield strength. This section results were originally reached by Musal in his pioneer work [18].

Here and in the previous Section, the material is treated as an isotropic solid. This approximation is sufficient for the purposes of the present analysis, as it allows us to demonstrate that the nanosecond laser pulses used in our experiments do not generate high pressure waves — only weak acoustic perturbations are produced, which are incapable of inducing plastic deformation. However, heating of the subsurface layer does create shear stresses high enough to drive plastic flow. Under these conditions, the deformation of the material proceeds in a quasi-static regime. Since such are regime is realized in our experiment, then it is used in the following Sections to investigate an anisotropic realistic crystal with the orientation-dependent properties. It will be demonstrated that the temperature rise required for plastic response depends on the crystallographic orientation of the copper grain.

VI. ORIENTATION DEPENDENCE OF THERMAL EXPANSION OF A SINGLE-CRYSTAL PLATE

The experimental results presented in Secs. II,III reveal a strong concentration of deformations at the joints of adjacent grains — see Figs. 1,2 clearly showing the grain boundaries after irradiation. The reasons for this concentration will become clear from the results presented here in this Section and in next Sections with atomistic simulations polycrystals.

The adjacent grains in a polycrystal have a large angle of misorientation. Consider the boundary line between adjacent grains in the sample plane. Due to large-angle misorientation, the Euler angles that define the orientation of lattice relative to the sample experience strong jumps when passing from one grain to another.

When heated, the strains in the plane of the free boundary are zero, but the stresses in the plane of this boundary are finite with amplitudes proportional to the change in temperature ΔT in the linear elasticity theory.

It is demonstrated below that the stresses strongly depend on the Euler angles for a fixed ΔT of uniform heating. That is, the stresses in adjacent crystallites will be very different if the grain boundary is fixed. Under conditions of elastostatics, the spatial distribution of elastic forces is uniform, which is achieved by deformation of the grain boundary. Thus, the dependence of stresses in a single crystallite on the Euler angles is a key for understanding the reasons of deformation concentration at the grain boundaries.

To demonstrate this dependence, we calculate the deformations and stresses in an infinite copper plate of single cubic crystal upon uniform heating with the linear elasticity theory. Heating starts from the room temperature of 300 K, but must not reach the melting point. Let a Cartesian coordinate system XYZ be attached to the crystal lattice with axes along the cube edges [100], [010], and [001]. In addition to this Cartesian system a corresponding spherical coordinate system is defined as shown in Fig. 10.

An arbitrary direction in the spherical coordinates is defined by the polar angle θ (measured from the Z-axis) and the azimuthal angle ϕ (see Fig. 10). Then a unit vector along this arbitrary direction is

$$\mathbf{n}_3 = (\sin\theta\cos\phi,\ \sin\theta\sin\phi,\ \cos\theta).$$

We now consider a planar plate cut from a single crystal with arbitrary orientation determined by the vector $\mathbf{n}_3$ as shown in Fig. 10. This vector is normal to the free plate surface illustrated by a green oval. The relative orientation of the plate and the crystal is given by the angles θ and ϕ. Consider the axis defined by the unit vector $\mathbf{n}_2 = (\sin\phi, -\cos\phi, 0)$. The vector $\mathbf{n}_2$ is perpendicular to the plane formed by the Z axis and $\mathbf{n}_3$; indeed, the dot product $\mathbf{n}_2\cdot\mathbf{n}_3$ vanishes. By definition of the Cartesian system x, y, z, $\mathbf{n}_2$ is orthogonal to the

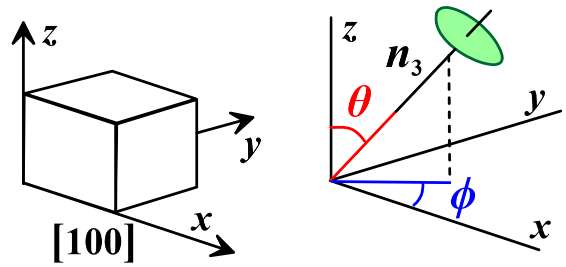

FIG. 10: Left: a unit cubic cell of the FCC copper lattice and the Cartesian coordinate system attached to the cell. Right: a corresponding spherical coordinate system with polar angle θ and azimuthal angle ϕ. The green oval indicates a piece of the free surface of the plate cut from a single crystal with the unit cell shown on the left. The vector $\mathbf{n}_3$ is perpendicular to the plate surface.

Z axis. A rotation by an angle θ about the $\mathbf{n}_2$ axis connects the Cartesian coordinate systems of the crystal and the plate. Under this rotation, the Z axis of the crystal aligns with $\mathbf{n}_3$.

We compute the free relative deformation along $\mathbf{n}_3$ upon heating under the condition that there are no displacements in the plane perpendicular to this direction. In addition to $\mathbf{n}_2$, we introduce a vector $\mathbf{n}_1 = (-\cos\theta\cos\phi, -\cos\theta\sin\phi, \sin\theta)$ so that $\mathbf{n}_1$, $\mathbf{n}_2$, $\mathbf{n}_3$ form an orthonormal set. Any unit vector in the plane spanned by $\mathbf{n}_1$ and $\mathbf{n}_2$ can be described by an angle ψ and has the form

$$\begin{aligned}\mathbf{n}(\psi) = (&-\cos\theta\cos\phi\cos\psi + \sin\phi\sin\psi,\\ &-\cos\theta\sin\phi\cos\psi - \cos\phi\sin\psi, \sin\theta\cos\psi).\end{aligned} \tag{9}$$

Introducing the strain tensor u_{ik} in the x, y, z coordinates $(i, k = x, y, z)$, the relative elongation along $\mathbf{n}(\psi)$ in the $\mathbf{n}_1, \mathbf{n}_2$ plane is $\xi(\psi) = u_{ik}n_i(\psi)n_k(\psi)$, where summation over repeated indices is implied. The requirement that these elongations vanish for all ψ yields three equations for the strain components u_{ik}:

$$\begin{aligned}&u_{xx}\sin^2\phi - u_{xy}\sin 2\phi + u_{yy}\cos^2\phi = 0 \\ &u_{xx}\cos^2\theta\cos^2\phi + u_{xy}\cos^2\theta\sin 2\phi - u_{xz}\sin 2\theta\cos\phi + \\ &+ u_{yy}\cos^2\theta\sin^2\phi - u_{yz}\sin 2\theta\sin\phi + u_{zz}\sin^2\theta = 0 \\ &u_{xx}\cos\theta\sin 2\phi - 2u_{xy}\cos\theta\cos 2\phi - 2u_{xz}\sin\theta\sin\phi - \\ &- u_{yy}\cos\theta\sin^2\phi + 2u_{yz}\sin\theta\cos\phi = 0\end{aligned} \tag{10}$$

We now incorporate the condition of free expansion of the crystal in the $\mathbf{n}_3$ direction upon a temperature variation ΔT. Since the cubic crystals behave like isotropic solids with respect to thermal expansion and can be characterized simply by the volumetric expansion coefficient α, the condition of zero stress in the $\mathbf{n}_3$ direction can be written as

$$(-P_T\delta_{ik} + \sigma_{ik})n_{3,k} = 0,$$

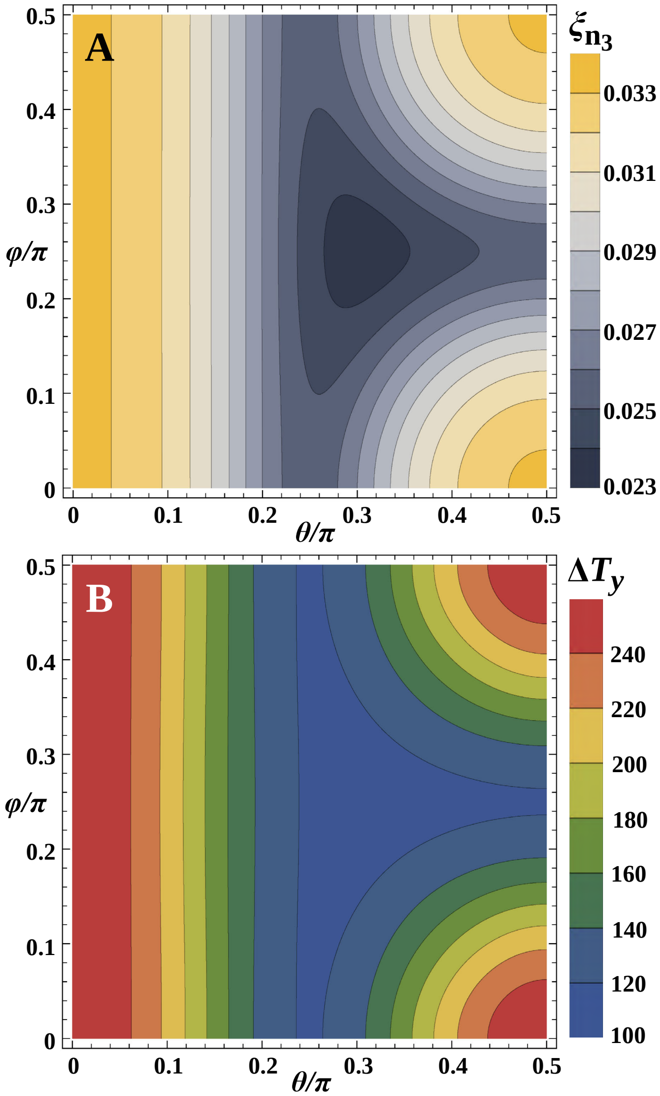

FIG. 11: A) Contour map of the relative displacement $\xi_{\mathbf{n_3}}(\theta, \phi)$ along the normal direction $\mathbf{n}_3$ to the single crystal copper plate calculated by Eq. 16 with fixed heating by $\Delta T = 800\,\mathrm{K}$. B) Temperature rise $\Delta T_y(\theta, \phi)$ in kelvins required for plastic response of copper calculated by Eq. 18 with the fixed yield strength $\sigma_y = 0.5\,\mathrm{GPa}$. The minimal temperature variation is achieved at the most stiff crystal orientation $\mathbf{n_3} = [\mathbf{111}]$.

where the sum in parentheses is a full stress tensor similar to that defined in Eq. (4). It consists of the thermal pressure $P_T = K\alpha\Delta T$ depending on the isothermal bulk modulus K, and the Hooke's law stress tensor σ_{ik} linearly depending on the strain tensor as $\sigma_{ik} = C_{ikjl}u_{jl}$, where C_{ikjl} is a stiffness tensor of elastic material.

Introducing the elastic moduli of cubic copper: $c_1 = C_{xxxx} = c_{11} = 168$ GPa, $c_2 = C_{xxyy} = c_{12} = 121$ GPa, $c_4 = C_{xyxy} = c_{44} = 75\,\mathrm{GPa}$, the stress components in the Hookean regime are

$$
\begin{aligned}
\sigma_{xx} &= c_1 u_{xx} + c_2(u_{yy} + u_{zz}) \\
\sigma_{yy} &= c_1 u_{yy} + c_2(u_{xx} + u_{zz}) \\
\sigma_{zz} &= c_1 u_{zz} + c_2(u_{xx} + u_{yy}) \\
\sigma_{ik} &= 2c_4 u_{ik}, \qquad i \neq k
\end{aligned}
$$

The condition of zero stress in the $\mathbf{n}_3$ direction gives three additional equations:

$$
\begin{aligned}
&[-P_T + c_1 u_{xx} + c_2(u_{yy} + u_{zz})] \sin\theta\cos\phi + \\
&\quad + 2c_4(u_{xy}\sin\theta\sin\phi + u_{xz}\cos\theta) = 0,
\end{aligned} \tag{11}
$$

$$
\begin{aligned}
&[-P_T + c_1 u_{yy} + c_2(u_{xx} + u_{zz})] \sin\theta\sin\phi + \\
&\quad + 2c_4(u_{xy}\sin\theta\cos\phi + u_{yz}\cos\theta) = 0,
\end{aligned} \tag{12}
$$

$$
\begin{aligned}
&[-P_T + c_1 u_{zz} + c_2(u_{xx} + u_{yy})] \cos\theta + \\
&\quad + 2c_4(u_{xz}\sin\theta\cos\phi + u_{yz}\sin\theta\sin\phi) = 0
\end{aligned} \tag{13}
$$

Solving the system of equations (10–13) yields the six strain components u_{xx}, u_{yy}, u_{zz}, u_{xy}, u_{xz}, u_{yz}. For convenience, we introduce the following quantities:

$$
\begin{aligned}
c_0 &= c_1 - c_2 - 2c_4 \\
u_1 &= c_1 - c_2 + c_4(\tan^2\theta - 1) \\
u_2 &= 2c_0 \sin^2\theta \sin^2\phi \cos^2\phi + c_4 \\
A_1 &= c_1 + c_4\tan^2\theta + \\
&\quad + \frac{u_1 u_2 (c_2 + c_4)\sin^2\theta}{(c_0\sin^2\theta\cos^2\phi + c_4)(c_0\sin^2\theta\sin^2\phi + c_4)}
\end{aligned} \tag{14}
$$

$$
\begin{aligned}
A_2 &= \cos^2\theta + \big(u_1 u_2 \sin^4\theta + \sin^2\theta \times \\
&\quad \times [(2c_0(c_1 - c_2 - c_4) - c_0^2\sin^2\theta)\times \\
&\quad \times \sin^2\theta\sin^2\phi\cos^2\phi + c_4(c_1 - c_2)]\big) / \\
&\quad / \left[(c_0\sin^2\theta\cos^2\phi + c_4)(c_0\sin^2\theta\sin^2\phi + c_4)\right]
\end{aligned} \tag{15}
$$

Then

$$
\begin{aligned}
u_{zz} &= P_T/A_1 \\
\frac{u_{xx}}{u_{zz}} &= \frac{u_1\sin^2\theta\cos^2\phi}{c_0\sin^2\theta\cos^2\phi + c_4} \\
\frac{u_{yy}}{u_{zz}} &= \frac{u_1\sin^2\theta\sin^2\phi}{c_0\sin^2\theta\sin^2\phi + c_4} \\
\frac{u_{xy}}{u_{zz}} &= \frac{1}{2}\frac{u_1\sin^2\theta\sin\phi\cos\phi\,(c_0\sin^2\theta + 2c_4)}{(c_0\sin^2\theta\cos^2\phi + c_4)(c_0\sin^2\theta\sin^2\phi + c_4)} \\
\frac{u_{xz}}{u_{zz}} &= \frac{1}{2}\tan\theta\cos\phi\frac{c_1 - c_2 - c_0\sin^2\theta\sin^2\phi}{c_0\sin^2\theta\cos^2\phi + c_4} \\
\frac{u_{yz}}{u_{zz}} &= \frac{1}{2}\tan\theta\sin\phi\frac{c_1 - c_2 - c_0\sin^2\theta\cos^2\phi}{c_0\sin^2\theta\sin^2\phi + c_4}
\end{aligned}
$$

Finally the relative elongation along $\mathbf{n}_3$ can then be written as

$$
\begin{aligned}
&\xi_{\mathbf{n_3}}(\theta,\phi) = u_{ik} n_{3,i} n_{3,k} = P_T A_2/A_1 = \\
&= u_{xx}\sin^2\theta\cos^2\phi + u_{xy}\sin^2\theta\sin 2\phi + u_{xz}\sin 2\theta\cos\phi + \\
&+ u_{yz}\sin 2\theta\sin\phi + u_{yy}\sin^2\theta\sin^2\phi + u_{zz}\cos^2\theta.
\end{aligned} \tag{16}
$$

The relative displacement $\xi_{\mathbf{n}_3}(\theta,\phi)$ for a copper sample with bulk modulus $K=(c_1+2c_2)/3=137$ GPa and volumetric thermal expansion coefficient $\alpha=51\times10^{-6}\,\mathrm{K}^{-1}$ is shown in Fig. 11(A) as a contour map.

The von Mises equivalent stress $\sigma_e=\sqrt{3J_2}$ [53] is defined via the second invariant of the stress deviator J_2

$$J_2(\theta,\phi)=\frac{1}{6}\left[(\sigma_{xx}-\sigma_{yy})^2+(\sigma_{xx}-\sigma_{zz})^2+(\sigma_{yy}-\sigma_{zz})^2\right] + (\sigma_{xy}^2+\sigma_{xz}^2+\sigma_{yz}^2). \tag{17}$$

It is possible to obtain a linear dependence of the equivalent stress on the thermal pressure (temperature variation) using the strains derived above:

$$\sigma_e=\frac{P_T}{\sqrt{2}A_1}\left[24c_4^2\frac{u_{xy}^2+u_{xz}^2+u_{yz}^2}{u_{zz}^2}+(c_1-c_2)^2\times \right. \tag{18}$$
$$\left.\times\left(\left(\frac{u_{xx}}{u_{zz}}-\frac{u_{yy}}{u_{zz}}\right)^2+\left(\frac{u_{xx}}{u_{zz}}-1\right)^2+\left(\frac{u_{yy}}{u_{zz}}-1\right)^2\right)\right]^{1/2}$$

The obtained dependence allows us to determine the necessary temperature variation ΔT_y at which the specified yield strength is reached $\sigma_e=\sigma_y$. It appears that such a temperature rise $\Delta T_y(\theta,\phi)$ depends not only on the value of σ_y, but also on the orientation of crystal according to Eq. (18).

It should be noted that the dynamic yield strength may be significantly higher than the static one under fast heating producing the enough high strain rate, such as $\sim 10^7\ \mathrm{s}^{-1}$ achieved with the nanosecond laser pulses, as it is discussed in Appendix. Taking into account a fairly high static yield strength of copper $\sigma_y=0.5\,\mathrm{GPa}$, which can be achieved at the high strain rates, the required temperature rise $\Delta T_y(\theta,\phi)$ falls into the range of 100 to 250 K (i.e. heating up to $T\approx 650\mathrm{K}$), as seen on the contour map presented in Fig. 11(B). Thus, some plastic transformations must occur at an arbitrary orientation $\mathbf{n_3}$ of crystal lattice by non-melting heating of the copper plate.

From the above analytical conclusions, it is clear that a similar formula derivation for a polycrystalline plate consisting of only two crystalline grains of different orientations is too difficult. Moreover, a purely mechanical description of the grain interaction is virtually incorrect, since such approach cannot take into account the inherent movement of grain boundaries, which results in changing the mass of grains, their formation and disappearance. Therefore, for a more realistic representation of plastic processes in polycrystals during nanosecond heating and cooling, we have performed molecular dynamics simulations presented in the following Section VII.

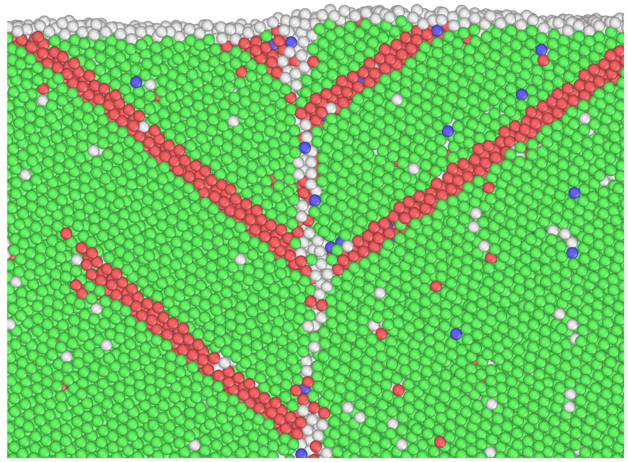

FIG. 12: Atomic structure of surface layer of the small copper bicrystal sample. Green atoms have a local environment characteristic of the FCC structure, red atoms correspond to the HCP structure (i.e., atoms belonging to deformation twins), and gray atoms have disordered neighborhood since they are located at the free surface or within the grain boundary.

VII. MD SIMULATION OF POLYCRYSTALS UNDER THERMOCYCLING

Based on the experimental results, it is established that the amplitude of the surface relief formed on copper surface and characterized by its roughness R_z, increases with the number of laser pulses. It is hypothesized that the relief development is caused by thermocycling of a thin surface layer exposed to laser pulse heating from room temperature up to approximately $0.9T_m$, i.e., not exceeding the melting temperature T_m, while the material surrounding the laser focal spot remains virtually cold.

To test this conjecture, two molecular dynamics simulations were performed using two different embedded-atom method (EAM) potentials for copper: one proposed by Mishin et al. [54] and another developed by Zhakhovsky [55]. The latter interatomic potential was optimized to model copper in a wide range of pressures and temperatures, which may arise as a result of laser pulse heating.

For the first MD simulation, a small copper sample was created using the Atomsk software [56] in order to reproduce a twin boundary between grains observed experimentally with transmission electron microscopy (Fig. 3). A crystal unit cell was constructed with the lattice axis $[11\bar{1}]$ along the Z-axis of sample, the $[2\bar{1}1]$ along the Y-axis, and the $[011]$ along the X-axis. A model bicrystal of size $L_z=64\,\mathrm{nm}$, $L_y=6.6\,\mathrm{nm}$, and $L_x=26\,\mathrm{nm}$ was built with the centers of the two grains located at $0.5\times0.5\times0.25$ and $0.5\times0.5\times0.75$ positions in units of the sample sizes. Then those crystallites were rotated about the Y-axis by -32° and 32°, respectively. The period-

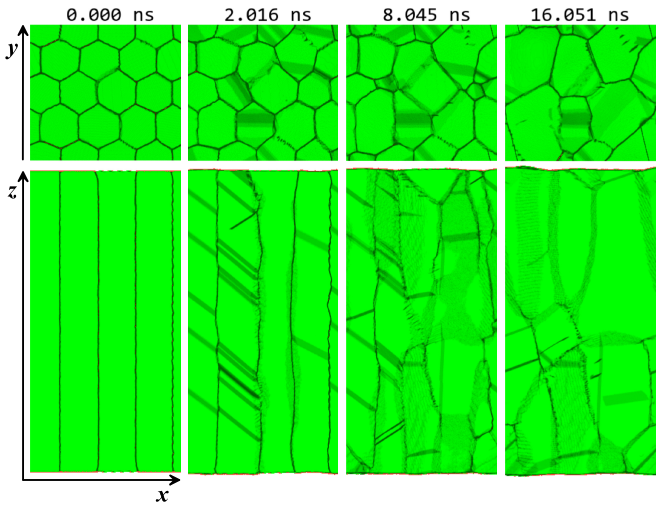

FIG. 13: Evolution of the averaged centrosymmetry parameter of local atomic order in the large polycrystalline copper sample under thermocycling. Maps of cooled polycrystal in XY and XZ cross sections are shown only after 1, 4, and 8 heating–cooling cycles. It can be seen that the initial highly ordered network structure of grain boundaries is strongly deformed over time, with a tendency for the number of grains to decrease and their maximal size to increase. A corresponding Video with structure evolution during thermocyling is available online in Supplementary Material.

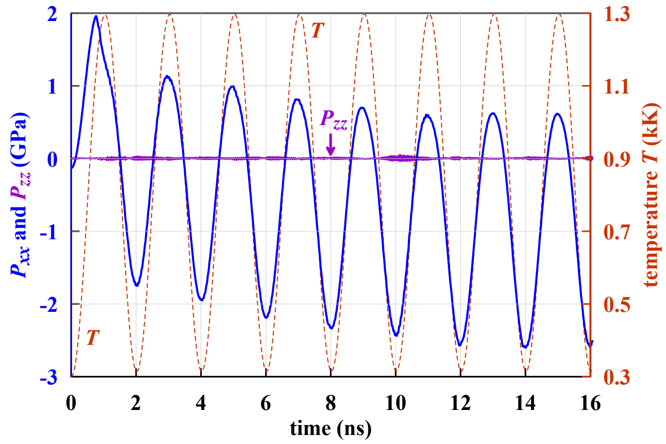

FIG. 14: Temperature $\langle T \rangle$ (dashed line), the transverse $\langle P_{zz} \rangle$ and the longitudinal $\langle P_{xx} \rangle$ components of the stress tensor, averaged over the central part of sample, during MD simulation of thermocycling using the Langevin thermostat only for the longitudinal components of atomic velocities v_x and v_y. Thermal expansion along the Z-axis is free, which results in $\langle P_{zz} \rangle \approx 0$.

ical conditions were imposed along the X and Y directions of the sample dimensions, while the free boundary condition is used for the positive Z direction and a potential wall at the negative Z boundary.

Next, the atomic positions were relaxed to the energy minimum and annealed at $T = 300$ K for 1 ns with the integration time step of 2 fs. The heating by a nonmelting laser pulse was modeled using a Nosé–Hoover thermostat with the target temperature of 1200 K during 1.4 ns.

MD simulation of the small sample described above was performed with the LAMMPS package [57] using the interatomic forces calculated by the EAM potential developed by Mishin [54]. Subsequent analysis and visualization of the obtained atomic structures were carried out using the OVITO software [58].

The formed deformation twins in such mirror grains are visible in Fig. 12, which are similar to those observed in the TEM image in Fig. 3. Because the grains are symmetric, the twin density per unit length of the grain boundary must be identical on both sides. But the height difference of about 1 nm between the adjacent grains was generated. Perhaps such difference arises from thermal fluctuations in atom motions, which may cause deformation to begin earlier in one of two grains.

An additional thermocycle, simulating the heating by laser pulse up to 1200 K followed by cooling to 300 K, does not lead to further relief development. This may be due to the small size of the grains, as well as the incomparability of nanosecond scale of simulation time with the real experimental laser pulse duration and time between pulses, which is much longer (by seven orders of magnitude), allowing stresses arisen after cooling to relax via slow diffusion processes.

For large-scale MD simulations, the EAM potential by Zhakhovsky [55] is used to calculate interatomic forces in copper. It was fitted with the stress-matching method [59] to provides a good agreement of the calculated cold stress-strain curves and other basic characteristics of solid with experimental data and DFT calculations. In particular, this potential gives the elastic constants $c_{11} = 176.1\,\mathrm{GPa}$, $c_{12} = 124.6\,\mathrm{GPa}$, $c_{44} = 84.3\,\mathrm{GPa}$ at $T = 0$, and the room temperature density $8.96\,\mathrm{g/cm^3}$ at $T = 293\,\mathrm{K}$. Also it provides the melting temperature $T_m = 1354\,\mathrm{K}$ in a good agreement with the experimental value of 1357.77 K.

An enlarged copper sample was created with dimensions $L_z = 120.3\,\mathrm{nm}$ along the free Z-axis, $L_x = 60\,\mathrm{nm}$ along the X axis, and $L_y = 54.2\,\mathrm{nm}$ along the Y-axis. Boundary conditions along X and Y are periodic, and the both sample sides at $z = \pm 60.2\,\mathrm{nm}$ are free.

The copper polycrystalline sample is generated with the Voronoi decomposition of the sample volume by setting positions of Voronoi centers. Each Voronoi subdomain contains a crystal grain having shape like a hex bar. Thus the whole sample consists of 16 elongated grains lengthwise the Z axis. They are combined together in a hexagonal cellular structure in the XY cross section as seen in Fig. 13 at 0 ns. The initial sides of grains $\approx 13\,\mathrm{nm}$ are slightly different since Voronoi positions are not perfectly correspond to a hexagonal lattice, so in or-

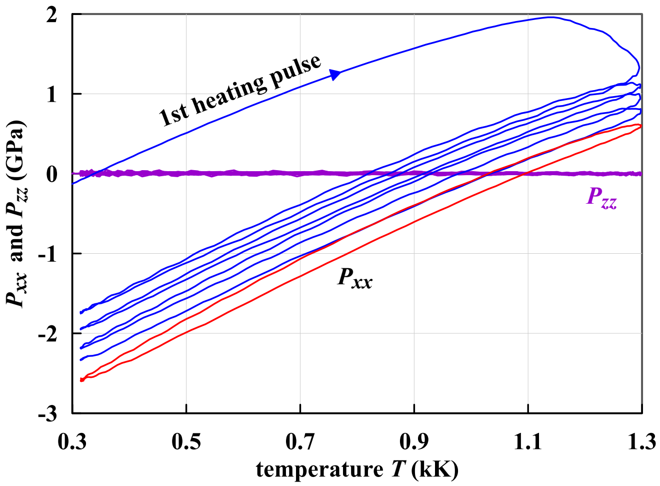

FIG. 15: Averaged longitudinal stress $\langle P_{xx} \rangle$ as a function of temperature for data taken from Fig. 14. This stress begins to decrease at the end of heating cycle, which contradicts the constant stress in the plastic regime shown in Fig. 9(f). The first four cycles are shown by the blue curve. Subsequent cycles almost ceased to change and hence only the last 8th cycle is shown by the red curve.

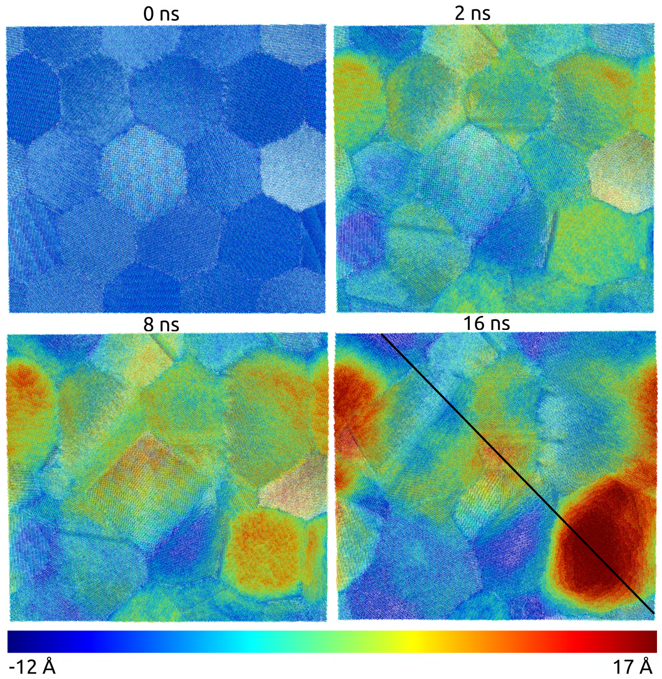

FIG. 16: Accumulation of the height difference along the Z-axis on the free surface of sample. The map of heights at $t = 0$ are obtained after the initial annealing before thermocycling. Subsequent maps are taken from fully cooled samples after 1 ($t = 2\,\mathrm{ns}$), 4 ($t = 8\,\mathrm{ns}$), and 8 ($t = 16\,\mathrm{ns}$) heating pulses. The last map shows the line along which the surface relief in Fig. 17 is constructed.

der to assemble such imperfect hex grains in a sample with the periodical conditions in XY-plane the sample axis length ratio is set close to $L_y/L_x = \sqrt{(3)}/2$. Initial orientations of the crystal axes in each grain are set randomly, which also yields the random mutual orientations of neighboring grains. The total number of atoms in the sample is about 33 millions, and the average number of atoms per grain is about two millions.

The resulting highly ordered polycrystalline sample was then annealed using the Langevin thermostat with $T = 600\,\mathrm{K}$ for 1 ns followed by slow cooling to $T = 300$ K in order to relax the non-equilibrium initial atomic configuration. This annealing leads to the generation of dislocations and slight migration of grain boundaries. Although the residual stress in the central part of cold sample was about $P_{xx} \approx P_{yy} \approx 0.12$ GPa, no dislocation motion or grain boundary migration was observed during $\sim 0.2\,\mathrm{ns}$ after cooling. Following the MD convention, the pressure tensor defined as $P_{i,k} = -\sigma_{i,k}$ is used in this Section, but we will refer to the pressure tensor components as stresses.

The distribution of the centrosymmetry parameter of atomic order [60] in a 4-nm-thick cross section near the top surface of sample is shown in Fig. 13 (top left) at the starting time $t = 0$ of thermocycling. It is interesting to examine the details of the subsequent evolution of the grain structure during thermocycling demonstrated in a Video provided in Supplementary Material. In particular, the grains are observed to enter the plastic regime asynchronously with increasing temperature since the dislocation activity and twinning starts earlier in some more yielding grains. This indicates variation of stiffness and yield strength of grains, which depends on their orientation, dislocation density, and likely on the types of grain boundaries surrounding them. In contrast the mirror grains shown in Fig. 12 have the same stiffness, which leads to synchronous twinning from the grain boundary.

During annealing, a height difference of about 0.4 nm formed on the initially nearly perfect free surface of the sample. After such initial preparation, the sample was subjected to thermocycling under conditions similar to pulsed laser heating with complete cooling to room temperature between the pulses. The time spent on sample preparation during the initial annealing was not counted, so the starting time of thermocycling simulation was set to zero.

A total of eight pulses were simulated and recorded. In the each cycle the sample was uniformly heated to the target temperature $T \approx 1300\,\mathrm{K} < T_m = 1354\,\mathrm{K}$ over approximately 1 ns and cooled to $T \approx 300\,\mathrm{K}$ eight times – between those limits the temperature was varied sinusoidally, as shown in Fig. 14.

Evolution of the longitudinal stress P_{xx} is also visible in this figure, which was averaged over the region $z \in [-30, 30]\,\mathrm{nm}$ in the central part of sample. Due to the free boundary conditions along Z-axis and the relatively

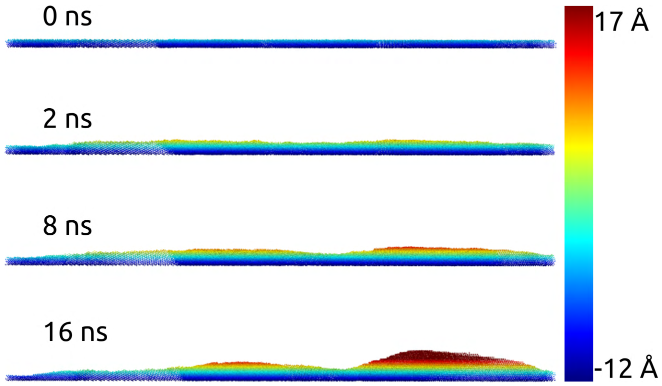

FIG. 17: Free surface relief along a straight line shown in Fig. 16. The vertical Z-heights are illustrated by a color scale relative to the initial surface position. The height is shown in a greatly enlarged vertical scale compared to the horizontal section length of about 70 nm.

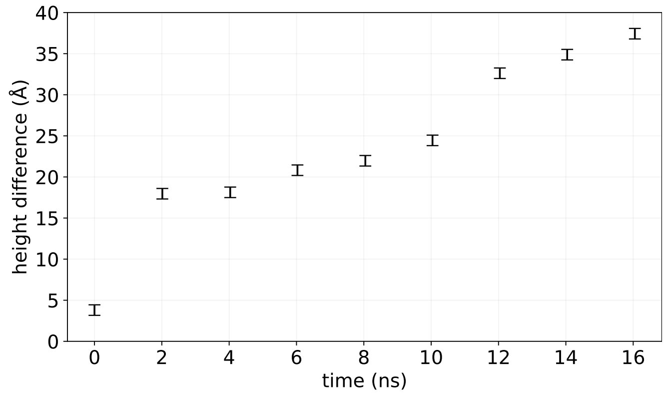

FIG. 18: Accumulation of the height difference measured after cooling in each cycle. The initial height difference is formed after preparation of sample for thermocycling. The growth of height difference becomes slower after 6th pulse.

long period of the heating–cooling cycle, the averaged transverse stress $\langle P_{zz}\rangle \approx 0$, as seen in Fig. 14. This indicates sufficiently slow heating, which may generate only very weak acoustic waves (here up to a few MPa).

Indeed, the heating and cooling times of 2 ns in each cycle are much longer than the acoustic time scale $L_z/c_s \approx 25$ ps, during which sound travels from one free side of the sample to the other side. Therefore, the motion occurs in the elastoplastic regime allowing the stresses to remain nearly constant across all cross sections of the sample and to follow the instantaneous temperature exactly. This allows the average pressure $\langle P\rangle = \frac{1}{3L_z}\int(P_{xx}+P_{yy}+P_{zz})dz$ over the whole sample to be defined explicitly. Thus, if the polycrystalline sample is considered as an isotropic solid with $\langle P_{xx}\rangle \approx \langle P_{yy}\rangle$, then the average shear stress $\langle\tau\rangle = \frac{1}{2}[\langle P_{xx}\rangle - \langle P_{zz}\rangle] \approx \frac{1}{2}\langle P_{xx}\rangle \approx \frac{3}{4}\langle P\rangle$ changes significantly (as seen from Fig. 14 in the range $[-1.2, +1]$ GPa), causing rearrangement of crystallites and producing an increase in the surface height variation.

Grain boundaries, where atomic packing is much less ordered than in the crystal lattice, are easily identified by a significant drop in the centrosymmetry parameter (see Fig. 13 and the corresponding Video in Supplementary material). The motion of these boundaries becomes sufficiently fast to be observed in MD simulations as the temperature approaches the melting point. The observed rearrangement of grain geometry leads both to growth of some grains and to shrinkage or even complete disappearance of others. In our simulation, out of the initial 16 equal-sized grains, only 5 large grains and about 7 small grains remained after 8 heating–cooling cycles.

Upon cooling the grain boundaries gradually become immobile. Their positions are shown in Fig. 13 after cooling and reaching the minimum room temperature (just before the start of a new heating cycle). No motion of grain boundaries or dislocations within grains is detected over observation times of ~ 100 ps after cooling, even though the residual shear stress in the center of the sample exceeds 1 GPa. It should be noted that although the average normal stresses between grains are nearly identical to maintain mechanical equilibrium during slow heating, the local stresses at each atom experience significant thermal fluctuations, especially in regions where lattice order is disrupted, such as grain boundaries and solid surface.

The MD results can also be presented in a stress–temperature plane as shown in Fig. 15. It can be seen that the longitudinal stress P_{xx} starts from a slightly pre-stressed state that arose during the initial annealing of the original sample. In the first heating cycle, the stress increases with temperature in an increasingly nonlinear manner and unexpectedly begins to decrease sharply at $T = 1150$ K. Such behavior, namely temporary overstressing of the material followed by relaxation kinetics, is not consistent with the conventional elastic-plastic models. Possibly our initial sample was not sufficiently annealed before thermal cycling — maybe it was too hardened because of an unrealistic initial configuration of grain boundaries. Interestingly, in the subsequent five cycles, the loops in the stress–temperature plane become significantly narrower than in the first cycle, but the loops continue to gradually drift toward larger residual stresses $P_{xx} < 0$ after each cooling. Starting from about the 6th pulse, this drift stops and the residual stresses saturate.

Comparison of the loops obtained from MD simulations (Fig. 15) with those calculated by the continuum method in Section V shows that plasticity in the polycrystalline layer begins at a stress approximately twice as high as in an isotropic layer with the assumed yield strength of 0.5 GPa. Moreover, the MD loops do not appear to undergo a plastic stage during cooling, which evolves in the purely elastic regime as seen in Fig. 15,

It turned out that 8 pulses were sufficient for this poly-

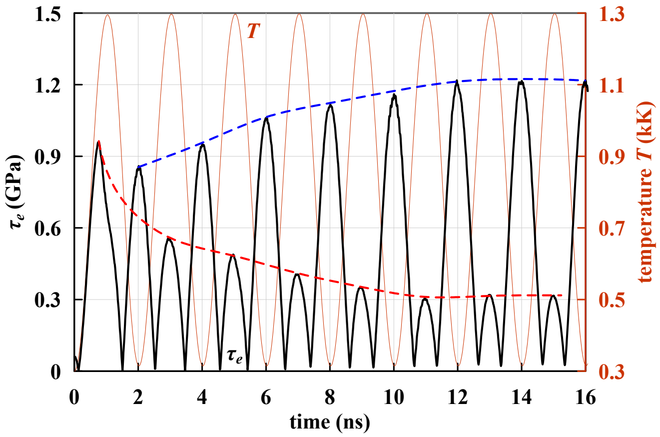

FIG. 19: Equivalent shear stress τ_e averaged over the central part of sample within $-30 < z < 30\,\text{nm}$. The dashed red envelope shows the maximal τ_e reached during the heating stages, while the higher residual shear stress τ_e after each cooling stage is indicated by the dashed blue envelope.

crystal configuration for the height difference to almost reach a certain saturation level, beyond which it does not increase further. However, in the real experiment, the accumulation of height difference was observed even after 15 pulses. It was found that the growth of protrusions and deepening of valleys does not occur over the entire surface of sample but only in some regions. Figure 16 shows the shape of the surface after each cooling. The inhomogeneity of uplift is also visible on the surface of individual grains — the uplift is greater than in others in some places of a single grain. Overall, the same regions of the solid surface grow or sink during thermocycling.

A side view of the growth of the height difference is presented in Fig. 17, for which vertical cross section of the near-surface layer of the sample is taken along a straight line indicated in Fig. 16, which passes through the region of maximum surface uplift. Figure 18 shows the dynamics of the height difference accumulation in the large MD sample having the small initial roughness $R_z \sim 0.4\,\text{nm}$ due to annealing. The experimental sample also has the initial roughness $R_z \sim 15\,\text{nm}$.

In our simulation the sample deforms along the Z-axis because changes in linear dimensions in other directions are not allowed due to periodic boundary conditions. This mimicks nearly uniaxial thermal expansion in the laser-heated spot whose heated depth is much smaller than its radius. It is also clear that the surface layer of the polycrystalline copper sample in the laser spot is subjected to shear stresses arising from uniaxial thermal expansion or contraction due to heating or cooling. If this stress exceeds the yield strength, which is specific to each grain and depends on its orientation and the density of dislocations accumulated in it, the plastic deformation begins in such crystallite. The shear stress is then relieved in the surrounding grains because an unloading shear wave propagates from the plastically deforming grain. It is precisely the difference in elastic-plastic response of adjacent grains is responsible for accumulation of surface height differences.

Evolution of the equivalent shear stress, defined as $\tau_e = \sigma_e/2$ via Eq.(17) during the uniform thermocycling is shown in Fig. 19. The calculated shear stresses in the cold sample are seen to be larger than those in the hot sample because a smaller shear stress is required for plastic deformations in the hot crystal.

Both the height difference and the stresses tend to reach a constant level after a certain number of heating–cooling cycles. This means that the sample grains eventually cease to respond plastically to the applied shear stresses. In our simulation, the polycrystal ceased to respond after about 6 cycles. The shear stresses that arise during subsequent cycles are insufficient to cause noticeable plastic deformation over timescales of ~ 1 ns. However, the positions of grain boundaries continue to change slowly in the hot state when the shear stress amplitude reaches $\tau_e \sim 0.3\,\text{GPa}$, as seen in Fig. 19.

The distribution of residual stresses with respect to grain locations in the cold sample is shown in Fig. 20. The darkest green hue corresponds to $\tau_e \sim 0.1$ GPa — such values are found at the grain boundaries and along the most dislocation slip paths (thick light-gray bands in Fig. 20A). The relative orientation of the grains is shown in Fig. 20B, where the color of each grain depends on the orientation angle of its crystal lattice. This orientation may slightly change upon dislocation generation. The lightest green hue in Fig. 20C corresponds to $\tau \approx 1.2$ GPa. Such a large residual shear stress is found in some grains, but it apparently does not cause noticeable plastic deformation in the cold state. Hardening of the material resulting in an increase in the yield strength has likely occurred due to increased dislocation density and the rearrangement of these grains.

It is interesting to note that the density of cold sample at $T = 300\,\text{K}$ decreases during thermocycling from 8.92 to $8.81\,\text{g/cm}^3$ along with the corresponding drop of pressure from zero to $-1.6\,\text{GPa}$. The volumetric thermal expansion coefficient (CTE), calculated using the obtained $\rho(T)$ curve at $T = 300\,\text{K}$, drops from $34 \cdot 10^{-6}$ to $30 \cdot 10^{-6}\,\text{K}^{-1}$. Such coefficient is notably lower than the thermal expansion coefficient $52 \cdot 10^{-6}\,\text{K}^{-1}$ provided by the used interatomic potential, because the pressure is rising during heating in our simulation. This observed decrease in CTE is consistent with the known grain size dependence of thermal expansion in copper: the CTE decreases with increasing grain size [61, 62].

VIII. CONCLUSIONS

This work presents a comprehensive experimental and theoretical study of the mechanisms of surface relief development on oxygen-free copper (99.999 %) samples heated by single and multiple nanosecond laser pulses

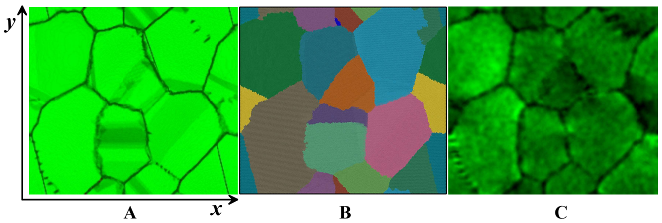

FIG. 20: Central cross sections of sample at 14 ns cooled after 7th heating pulse. A) map of centrosymmetry parameter, B) map of grains colored according their orientations, C) distribution of residual equivalent shear stress. The minimum stress $\tau_e \approx 0.1$ GPa corresponds to the darkest green hue and the maximum of 1.2 GPa is shown in the lightest hue.

with wavelength 355 nm and fluences $F = 0.6{-}1.05$ J/cm^2. Number of pulses was from 1 to 15, pulse duration 10 ns, and repetition rate of 10 Hz. At such low pulse fluences and repetition rate the copper surface was heated up to $\sim 0.9 T_m$ without melting, and each subsequent pulse irradiates a fully cooled surface.

In the considered fluence range it was established experimentally that there is a progressive accumulation of protrusion heights and depression depths near the grain boundaries as the number of laser pulses incident on the same spot increases. For a small number of pulses (1–3), the protrusion height at the grain boundary relative to the unirradiated surface is 40–70 nm, but it increases progressively with pulse number and may reach 500 nm for 10–15 pulses. Scanning electron microscopy reveals no signs of intense ablation at the periphery of the laser spot, confirming the dominant role of the thermoplastic deformation mechanism in relief development.

TEM/STEM analysis reveals a well-developed defect substructure in the surface layer of 200–500 nm thick: the nanoscale deformation twin plates, dislocation subboundaries, and low-angle subgrain boundaries with misorientations of $1{-}5^\circ$. Formation of deformation twinning and dislocation substructure, occurring simultaneously within a single thermomechanical heating–cooling cycle, indicates that the temperature in the surface layer during exposure significantly exceeded the activation threshold for high-temperature dislocation glide ($\approx [0.4 - 0.5] T_m$), without reaching the melting temperature. The EDX spectroscopy confirms that the chemical composition of the surface layer remained unchanged.

The conditions separating elastic and elastic–plastic response of copper were investigated with continuum modeling of laser heating utilizing a simple elastic–plastic model. In particular, the temperature variation T_y required to initiate plasticity was determined.

The theory developed in this work relates the development of surface height differences near grain boundaries to the dependence of the longitudinal stresses on the lattice orientation of grains with respect to the target surface under slow uniform heating. Misorientated grains are variously deformed to maintain mechanical equilibrium. The inequality of their stiffness coefficients and yield strengths, especially in the vicinity of grain boundaries, leads to the observed surface deformations localized along these boundaries. The transition from elastic to irreversible plastic deformation results in the retention of surface height differences as a residual spatially inhomogeneous deformation after cooling of the heated spot.

Molecular dynamics simulations reveals that the main mechanism of relief development is the difference in deformations of neighboring grains due to their different stiffnesses and yield strengths. Formation of deformation twins near the grain boundary, similar to those observed experimentally, was detected in the bicrystal simulation. Dislocations and deformation twins not only provide plastic deformation but also serve as channels for mass transfer near grain boundaries. Twinning occurs through collective transport of atomic layers: each partial Shockley dislocation shifts an entire atomic layer, and repeated passage of such dislocations leads to layer-by-layer twin thickening. MD simulation also demonstrates that the surface height differences are accumulated in neighbor grains during thermocycling.

The established patterns of relief formation and structural changes are of key importance for understanding the degradation mechanisms of metallic surfaces subjected to repetitive pulsed laser irradiation. In particular, the obtained results can be used to develop methods for improving the operational durability of laser mirrors.

The results have direct practical significance for understanding the physical mechanisms of surface degradation of copper contacts in microelectronic boards, mirrors of laser systems (“optical fatigue”), and can serve as a physically substantiated basis for developing methods to predict the lifetime and enhance the operational durability of high-power metal optics components, as well as other copper and copper-alloy products operating under cyclic pulsed thermomechanical loading.

SUPPLEMENTARY MATERIAL

See the Supplementary Video that shows the microstructure evolution of copper sample under thermocycling. Maps of centrosymmetry parameter of local atomic order obtained in MD simulation are used in the Video. Several maps are also presented in Fig. 13.

ACKNOWLEDGMENTS

The study of the fine structure of the surface copper layer by transmission electron microscopy and computer simulation of a copper bicrystal was supported by State Assignment No. FFSG-2024-0018 (State Registration No. 124020700089-3) (Yu.R.K., I.V.N., S.S.M.). The theoretical physics and mathematical modeling part was supported by the Landau Institute for Theoretical

Physics RAS under State Assignment No. FFWR-2024-0013 (State Registration No. 124041900014-8) (N.A.I., Yu.V.P., V.A.K.). The work was carried out with the financial support of the Ministry of Science and Higher Education of the Russian Federation (State Assignment No. 124022400174-3) (E.A.P.). The experimental work on laser exposure was carried out under State Assignment No. FFGR-2025-0001 (State Registration No. 126011915722-5) of the Institute of Electrophysics and Electric Power (IEE) RAS (T.V.M., Yu.V.Kh., V.E.R.).

AUTHOR DECLARATIONS

Conflict of Interest

The authors have no conflicts to disclose.

Author Contributions

Ivan Nelasov: Conceptualization (lead); Formal analysis (equal); Investigation (equal); Methodology (equal); Visualization (equal); Writing - original draft (equal); Writing - review & editing (equal). **Sergey Manokhin**: Investigation (equal); Visualization (equal); Writing - original draft (equal); Writing - review & editing (equal). **Yury Kolobov**: Formal analysis (equal); Investigation (equal); Writing - original draft (equal); Writing - review & editing (equal). **Vasily Zhakhovsky**: Formal analysis (lead); Investigation (equal); Software (lead); Visualization (equal); Writing - original draft (equal); Writing - review & editing (equal). **Sergey Grigoryev**: Investigation (equal); Visualization (equal); Writing - original draft (equal); Writing - review & editing (equal). **Evgeniy Perov**: Investigation (equal); Visualization (equal). **Yury Petrov**: Investigation (equal); Visualization (equal); Writing - original draft (equal). **Victor Khokhlov**: Software (equal); Visualization (equal); Writing - original draft (equal). **Nail Inogamov**: Formal analysis (equal); Investigation (equal); Visualization (equal); Writing - original draft (equal); Writing - review & editing (equal). **Vladislav Khomich**: Investigation (equal). **Taras Malinskiy**: Investigation (equal). **Vladimir Rogalin**: Investigation (equal); Writing - review & editing (equal).

DATA AVAILABILITY STATEMENT

Experimental data is available in the article, simulation data is available from the corresponding authors upon reasonable request.

APPENDIX

All continuum simulations in this work are performed with the following characteristics of copper. The density of copper is taken equal to $\rho_0 = 8930\,\mathrm{kg/m^3}$ at the initial room temperature, and the bulk sound speed is $c = 3980\,\mathrm{m/s}$, which gives the bulk modulus $K = \rho_0 c^2 = 141.5\,\mathrm{GPa}$. Since the Poisson ratio is assumed to be constant $\nu = 0.35$ for pure copper, then the shear modulus can be calculated as $G = K(3/2)(1-2\nu)/(1+\nu) = 47.2\,\mathrm{GPa}$. Thus, the Young's modulus $E = 9KG/(3K+G) = 127.3\,\mathrm{GPa}$, and the longitudinal sound speed in copper is $\sqrt{(K+(4/3)G)/\rho_0} = 4783\,\mathrm{m/s}$. The Grüneisen parameter is assumed to be constant $\Gamma = 1.943$. The heat capacity of solid copper is taken equal $385\,\mathrm{J/K/kg}$, and thermal conductivity is set equal to $401\,\mathrm{W/K/m}$ [63].

The reference curves used in the Mie–Grüneisen equation of state (3) are given by

$$P_r = \rho_0 c_0^2 \frac{1-x}{[1-s(1-x)]^2}, \quad e_r = \frac{P_r}{\rho_0}\frac{1-x}{2}, \tag{A1}$$

where $x = \rho_0/\rho$. The used parameters are presented above and linked with the volumetric thermal expansion coefficient α defined by the thermodynamic relation $\alpha = \Gamma\rho C_V/K = 47.2\cdot 10^{-6}\,\mathrm{K^{-1}}$, which is closed to the experimental $\alpha = 49.5\cdot 10^{-6}\,\mathrm{K^{-1}}$ at a room temperature [63].

To model the elastic–plastic response of material the symmetric stress tensor is decomposed into a spherical part and a deviatoric part: $\sigma_{ij} = -P\delta_{ij} + s_{ij}$, where the indices i,j correspond to the coordinates $\{x,y,z\}$, and δ_{ij} is the Kronecker delta. The components of the deviatoric stress tensor are determined according to the Hooke's law for elastic materials:

$$\frac{ds_{ij}}{dt} = 2G\frac{d\varepsilon_{ij}}{dt}, \tag{A2}$$

where ε_{ij} is the elastic strain tensor. For plastic materials, the calculated components s_{ij} are corrected according to the von Mises yield criterion using the equivalent stress σ_e:

$$s_{ij} = \begin{cases} s_{ij}, & \text{if } \sigma_e \le \sigma_y \\ s_{ij}\sigma_y/\sigma_e, & \text{if } \sigma_e > \sigma_y \end{cases}$$

The relatively high yield strength $\sigma_y = 500$ MPa is assumed in this work in contrast to the much lower $\sigma_y = 62$ MPa used in Ref. [18] for estimating the temperature rise required for plastic deformation. It is known [34] that the yield strength monotonically increases in metals with increasing temperature at strain rates above $10^4\,\mathrm{s^{-1}}$. During rapid heating by a laser pulse with a duration of 1–10 ns, the experimental strain rate is estimated to be $10^6{-}10^7\,\mathrm{s^{-1}}$, at which the dynamic yield strength becomes significantly higher than the static yield strength [30, 31]. Therefore, the temperature threshold for the onset of plastic processes will actually be higher than one estimated for relatively slower heating, which generates the strain rates below $10^4\,s^{-1}$.

[1] A. Kruusing, Underwater and water-assisted laser processing: Part 1—general features, steam cleaning and shock processing, Optics and Lasers in Engineering **41**, 307 (2004).

[2] S. J. Lainé, K. M. Knowles, P. J. Doorbar, R. D. Cutts, and D. Rugg, Microstructural characterisation of metallic shot peened and laser shock peened ti–6al–4v, Acta Materialia **123**, 350 (2017).

[3] S. J. Turneaure, P. Renganathan, J. M. Winey, and Y. M. Gupta, Twinning and dislocation evolution during shock compression and release of single crystals: Real-time x-ray diffraction, Phys. Rev. Lett. **120**, 265503 (2018).

[4] K. Ichiyanagi, S. Takagi, N. Kawai, R. Fukaya, S. Nozawa, K. Nakamura, K.-D. Liss, M. Kimura, and S.-i. Adachi, Microstructural deformation process of shock-compressed polycrystalline aluminum, Sci Rep **9**, 7604 (2019).

[5] C. Wang, L. Wang, C.-L. Wang, K. Li, and X.-G. Wang, Dislocation density-based study of grain refinement induced by laser shock peening, Optics Laser Technology **121**, 105827 (2020).

[6] L. Guan, Z.-X. Ye, X.-Y. Yang, J.-M. Cai, Y. Li, Y. Li, Y.-K. Zhang, and G. Wang, Pitting resistance of 316 stainless steel after laser shock peening: Determinants of microstructural and mechanical modifications, Journal of Materials Processing Technology **294**, 117091 (2021).

[7] S. Keller, S. Chupakhin, P. Staron, E. Maawad, N. Kashaev, and B. Klusemann, Experimental and numerical investigation of residual stresses in laser shock peened aa2198, Journal of Materials Processing Technology **255**, 294 (2018).

[8] N. A. Inogamov, V. A. Khokhlov, Y. V. Petrov, and V. V. Zhakhovsky, Hydrodynamic and molecular-dynamics modeling of laser ablation in liquid: from surface melting till bubble formation, Opt Quant Electron **52**, 63 (2020).

[9] Z. Li, Y. Zhang, Z. Zhang, Y.-T. Cui, Q. Guo, P. Liu, S. Jin, G. Sha, K. Ding, Z. Li, T. Fan, H. M. Urbassek, Q. Yu, T. Zhu, D. Zhang, and Y. M. Wang, A nanodispersion-in-nanograins strategy for ultra-strong, ductile and stable metal nanocomposites, Nature Communications **13**, 5581 (2022).

[10] V. Zhakhovsky, Yury Kolobov, S. Ashitkov, N. Inogamov, I. Nelasov, S. Manokhin, V. Khokhlov, D. Ilnitsky, Yury Petrov, A. Ovchinnikov, O. Chefonov, and D. Sitnikov, Shock-induced melting and crystallization in titanium irradiated by ultrashort laser pulse, Physics of Fluids **35**, 096104 (2023).

[11] F. Akhmetov, I. Milov, S. Semin, F. Formisano, N. Medvedev, J. M. Sturm, V. V. Zhakhovsky, I. A. Makhotkin, A. Kimel, and M. Ackermann, Laser-induced electron dynamics and surface modification in ruthenium thin films, Vacuum **212**, 112045 (2023).

[12] I. Nelasov, S. Manokhin, Y. Kolobov, V. Zhakhovsky, E. Perov, Y. Petrov, Y. Khomich, T. Malinsky, N. Inogamov, and V. Rogalin, Evolution of the microstructure of the near-surface copper layer during thermal cycling by nanosecond laser pulses, ZhETF (in Russian) **167**, 782 (2025).

[13] A. Tokmacheva-Kolobova, Investigation of the mechanism of nanostructuring of near-surface titanium layers under the influence of nanosecond laser pulses, Tech. Phys. Lett. **47**, 143 (2021).

[14] A. Y. Vorobyev and C. Guo, Direct femtosecond laser surface nano/microstructuring and its applications, Laser and Photonics Reviews **7**, 385 (2013).

[15] Y. R. Kolobov, M. Y. Smolyakova, A. Y. Kolobova, A. A. Ionin, S. I. Kudryashov, S. V. Makarov, P. N. Saltuganov, D. A. Zayarny, and A. E. Ligachev, Superhydrophylic textures fabricated by femtosecond laser pulses on sub-micro- and nano-crystalline titanium surfaces, Laser Physics Letters **11**, 125602 (2014).

[16] T. V. Malinskiy, S. I. Mikolutskiy, V. E. Rogalin, Y. V. Khomich, V. A. Yamshchikov, I. A. Kaplunov, and A. I. Ivanova, Plastic deformation of copper under the action of high-power nanosecond uv laser pulse, Technical Physics Letters **46**, 831 (2020).

[17] L. Li, X. Du, J. Chen, and Y. Wu, Thermal fatigue failure of micro-solder joints in electronic packaging devices: A review, Materials **17**, 10.3390/ma17102365 (2024).

[18] H. M. Musal, Jr., Thermomechanical stress degradation of metal mirror surfaces under pulsed laser irradiation, in *Laser Induced Damage in Optical Materials: 1979*, NBS Special Publication No. 568, edited by H. E. Bennett, A. J. Glass, A. H. Guenther, and B. E. Newnam (National Bureau of Standards, Boulder, CO, 1980) pp. 159–172.

[19] V. V. Apollonov, A. M. Prokhorov, V. Y. Khomich, and S. A. Chetkin, Thermoelastic action of pulse-periodic laser radiation on the surface of a solid, Soviet Journal of Quantum Electronics **12**, 188 (1982).

[20] R. A. Liukonen and A. M. Trofimenko, Dynamics of small-scale modifications of metallooptics mirror surface under pulse light loading, Zhurnal Tekhnicheskoi Fiziki **61**, 127 (1991), in Russian.

[21] F. Mirzoev, Propagation of nonlinear longitudinal waves in a solid with regard to the interaction between the strain field and the field of defects, Tech. Phys. **47**, 1258 (2002).

[22] T. V. Malinskiy and V. E. Rogalin, Prethreshold effects, when copper and its alloys were impacted to ultraviolet laser pulses, Tech. Phys. **67**, 211 (2022).

[23] Y. Khomich, T. Malinskiy, V. Rogalin, V. Yamshchikov, and I. Kaplunov, Modification of the surface of copper and its alloys due to impact to nanosecond ultraviolet laser pulses, Acta Astronautica **194**, 434 (2022).

[24] T. V. Malinskiy, V. E. Rogalin, and V. A. Yamshchikov, Plastic deformation of copper and its alloys under the action of nanosecond uv laser pulse, Physics of Metals and Metallography **123**, 178 (2022).

[25] T. V. Malinskii, V. E. Rogalin, V. Y. Shur, and D. K. Kuznetsov, Peculiarities of the behavior of point defects under the optoplastic effect in copper, Physics of Metals and Metallography **124**, 728 (2023).

[26] V. Rogalin, V. Zhakhovsky, N. Inogamov, Y. Kolobov, S. Manokhin, T. Malinsky, I. Nelasov, E. Perov,

Y. Petrov, V. Khokhlov, Y. Khomich, and A. Doludenko, Thermal cycling of the copper surface in preablation mode when heated by ultraviolet laser nanosecond pulses (in russian), Physics of the Solid State (FTT) **67**, 2371 (2025).

[27] I. V. Nelasov, A. I. Kartamyshev, A. O. Boev, A. G. Lipnitskii, Y. R. Kolobov, and T. K. Nguyen, Molecular dynamics simulation of the behavior of titanium under high-speed deformation, Modelling and Simulation in Materials Science and Engineering **29**, 065007 (2021).

[28] G. I. Kanel, S. V. Razorenov, and V. E. Fortov, *Shock-Wave Phenomena and the Properties of Condensed Matter* (Springer, 2004).

[29] G. I. Kanel', V. E. Fortov, and S. V. Razorenov, Shock waves in condensed-state physics, Phys. Usp. **50**, 771 (2007).

[30] R. J. Clifton, High strain rate behavior of metals, Applied Mechanics Reviews **43**, S9 (1990).

[31] M. Meyers, D. Benson, O. Vohringer, B. Kad, Q. Xue, and H.-H. Fu, Constitutive description of dynamic deformation: physically-based mechanisms, Materials Science and Engineering: A **322**, 194 (2002).

[32] S. I. Ashitkov, M. B. Agranat, G. I. Kanel', P. S. Komarov, and V. E. Fortov, Behavior of aluminum near an ultimate theoretical strength in experiments with femtosecond laser pulses, JETP Lett. **92**, 516 (2010).

[33] V. Zhakhovskii and N. Inogamov, Elastic-plastic phenomena in ultrashort shock waves, JETP Lett. **92(8)**, 521 (2010).

[34] E. B. Zaretsky and G. I. Kanel, Response of copper to shock-wave loading at temperatures up to the melting point, Journal of Applied Physics **114**, 083511 (2013).

[35] M. E. Povarnitsyn, P. R. Levashov, and D. V. Knyazev, Simulation of ultrafast bursts of subpicosecond pulses: In pursuit of efficiency, Applied Physics Letters **112**, 051603 (2018).

[36] A. Nakhoul, A. Rudenko, X. Sedao, N. Peillon, J. P. Colombier, C. Maurice, G. Blanc, A. Borbély, N. Faure, and G. Kermouche, Energy feedthrough and microstructure evolution during direct laser peening of aluminum in femtosecond and picosecond regimes, Journal of Applied Physics **130**, 015104 (2021).

[37] N. A. Inogamov, E. A. Perov, V. V. Zhakhovsky, V. V. Shepelev, Y. V. Petrov, and S. V. Fortova, Laser shock wave: The plasticity and thickness of the residual deformation layer and the transition from the elastoplastic to elastic propagation mode, JETP Lett. **115**, 71 (2022).

[38] R. Fabbro, J. Fournier, P. Ballard, D. Devaux, and J. Virmont, Physical study of laser-produced plasma in confined geometry, J. Appl. Phys. **68**, 775 (1990).

[39] N. Inogamov, V. Zhakhovsky, D. Ilnitsky, and V. Khokhlov, Picosecond-nanosecond laser flash, formation of powerful elastic waves in crystals, and shock peening, in *Proc. of the 32nd International Symposium on Shock Waves (ISSW32)* (ISSW32, 2019) pp. 3077–3106.

[40] C. Correa, D. Peral, J. Porro, M. Diaz, L. Ruiz de Lara, A. Garcia-Beltran, and J. Ocaia, Random-type scanning patterns in laser shock peening without absorbing coating in 2024-t351 al alloy: A solution to reduce residual stress anisotropy, Optics and Laser Technology **73**, 179 (2015).

[41] T. Kawashima, T. Sano, A. Hirose, S. Tsutsumi, K. Masaki, K. Arakawa, and H. Hori, Femtosecond laser peening of friction stir welded 7075-t73 aluminum alloys, Journal of Materials Processing Technology **262**, 111 (2018).

[42] Y. Lian, Y. Hua, J. Sun, Q. Wang, Z. Chen, F. Wang, K. Zhang, G. Lin, Z. Yang, Q. Zhang, and L. Jiang, Martensitic transformation in temporally shaped femtosecond laser shock peening 304 steel, Applied Surface Science **567**, 150855 (2021).

[43] Y. Li, Z. Ren, X. Jia, W. Yang, N. Nassreddin, Y. Dong, C. Ye, A. Fortunato, and X. Zhao, The effects of the confining medium and protective layer during femtosecond laser shock peening, Manufacturing Letters **27**, 26 (2021).

[44] V. V. Shepelev, Y. V. Petrov, N. A. Inogamov, V. V. Zhakhovsky, E. A. Perov, and S. V. Fortova, Attenuation and inflection of initially planar shock wave generated by femtosecond laser pulse, Optics & Laser Technology **152**, 108100 (2022).

[45] F. Siska, S. Forest, P. Gumbsch, and D. Weygand, Finite element simulations of the cyclic elastoplastic behaviour of copper thin films, Modelling and Simulation in Materials Science and Engineering **15**, S217 (2006).

[46] V. Alekseev, S. Batanov, I. Mitrichev, A. Karakhanov, A. Moksyakov, G. Ryabikova, and S. Filin, Method of preparing the optical surface of metal workpieces for deep drawing. Patent RU 2042456 (1995).

[47] E. Montoya, S. Bals, M. D. Rossell, D. Schryvers, and G. Van Tendeloo, Evaluation of top, angle, and side cleaned FIB samples for TEM analysis, Microscopy Research and Technique **70**, 1060 (2007).

[48] Y. Petrov, S. Romashevskiy, A. Dyshlyuk, V. Khokhlov, E. Eganova, M. Polyakov, S. Evlashin, S. Ashitkov, O. Vitrik, and N. Inogamov, Abnormal transmission of light by optically thick nickel films, which are optoacoustic transducers (in russian), ZhETF **167**, 645 (2025).

[49] S. S. Makarov, V. V. Zhakhovsky, S. Y. Grigoryev, P. Chuprov, T. A. Pikuz, *et al.*, Formation of high-aspect-ratio nanocavity in LiF crystal using a femtosecond X-ray free-electron laser pulse, Nature Communications **16**, 11504 (2025).

[50] A. Dyshlyuk, S. Romashevskiy, Y. Petrov, V. Khokhlov, O. Vitrik, and N. Inogamov, Simulation of brillouin oscillations generated by a metamaterial based on a nanostructured nickel film (in russian), Pis'ma ZhETF **123** (2026).

[51] M. L. Wilkins, *Computer simulation of dynamic phenomena* (Springer Berlin, Heidelberg, 1999).

[52] L. D. Landau, E. M. Lifshitz, A. M. Kosevih, and L. P. Pitaevslii, *Theory of Elasticity* (Elsevier, 1986).

[53] S. Timoshenko and J. N. Goodier, *Theory of Elasticity*, 3rd ed. (McGraw-Hill Book Company, Inc., New York, 1970).

[54] Y. Mishin, M. J. Mehl, D. A. Papaconstantopoulos, A. F. Voter, and J. D. Kress, Structural stability and lattice defects in copper: Ab initio, tight-binding, and embedded-atom calculations, Phys. Rev. B **63**, 224106 (2001).

[55] V. V. Zhakhovsky, EAM potential for Copper is available for download, look also https://openkim.org.

[56] P. Hirel, Atomsk: A tool for manipulating and converting atomic data files, Computer Physics Communications **197**, 212 (2015).

[57] A. P. Thompson, H. M. Aktulga, R. Berger, D. S. Bolintineanu, W. M. Brown, P. S. Crozier, P. J. in 't Veld, A. Kohlmeyer, S. G. Moore, T. D. Nguyen, R. Shan, M. J. Stevens, J. Tranchida, C. Trott, and S. J. Plimpton, LAMMPS - a flexible simulation tool for particle-based

materials modeling at the atomic, meso, and continuum scales, Comp. Phys. Comm. **271**, 108171 (2022).

[58] A. Stukowski, Visualization and analysis of atomistic simulation data with OVITO–the open visualization tool, Modelling and Simulation in Materials Science and Engineering **18**, 015012 (2009).

[59] V. V. Zhakhovskii, N. A. Inogamov, Y. V. Petrov, S. I. Ashitkov, and K. Nishihara, Molecular dynamics simulation of femtosecond ablation and spallation with different interatomic potentials, Appl. Surf. Sci. **255**, 9592 (2009).

[60] S. Murzov, S. Ashitkov, E. Struleva, P. Komarov, V. Zhakhovsky, V. Khokhlov, and N. Inogamov, Elasto-plastic and polymorphic transformations of iron at ultra-high strain rates in laser-driven shock waves, Journal of Applied Physics **130**, 10.1063/5.0076869 (2021).

[61] S. Hwang and Y. Kim, The effect of grain size and film thickness on the thermal expansion coefficient of copper thin films, Journal of Nanoscience and Nanotechnology **11**, 1555 (2011).

[62] P. A. T. Olsson, I. Awala, J. Holmberg-Kasa, A. M. Krause, M. Tidefelt, O. Vigstrand, and D. Music, Grain size-dependent thermal expansion of nanocrystalline metals, Materials **16**, 5032 (2023).

[63] J. R. Rumble, ed., *CRC Handbook of Chemistry and Physics*, 99th ed. (CRC Press, Boca Raton, FL, 2018).